

303421  
Pg. 73

FINAL REPORT  
FOR  
DELIVERY ORDER 14/NAS8-36955

**MODELLING CRYSTAL GROWTH:  
CONVECTION IN AN ASYMMETRICALLY HEATED  
AMPOULE**

PRINCIPAL INVESTIGATORS

J. IWAN D. ALEXANDER AND FRANZ ROSENBERGER

CO-INVESTIGATORS

J. P. PULICANI

S. KRUKOWSKI

JALIL OUAZZANI

CENTER FOR MICROGRAVITY AND MATERIALS RESEARCH  
THE UNIVERSITY OF ALABAMA IN HUNTSVILLE

(NASA-CR-184214) MODELLING CRYSTAL GROWTH:  
CONVECTION IN AN ASYMMETRICALLY HEATED  
AMPOULE Final Report (Alabama Univ.) 73 p  
CSCL 20L

N92-10676

Unclas  
G3/76 0303421

## TABLE OF CONTENTS

	Page
1. GENERAL	1
2. INTRODUCTION: CONVECTION IN AN ASYMMETRICALLY HEATED CYLINDER	1
3. FORMULATION OF THE PROBLEM	2
4. NUMERICAL METHOD	5
5. RESULTS	9
6. DISCUSSION AND SUMMARY	11
7. REFERENCES	12
8. FIGURE CAPTIONS AND FIGURES	14
9. APPENDIX 1:	28
A Fourier-Chebyshev Pseudo-Spectral method for Solving Steady 3D Navier-Stokes and Heat Equations in Cylindrical Cavities, by J. P. Pulicani and J. Ouazzani	

## 1. GENERAL

Recently, non-axisymmetric convection in (vertical) directional solidification experiments has been observed. It has been suggested that the flow character is a consequence of the lack of azimuthal symmetry in the temperature field. Motivated by these observations we have examined the consequences of deviations from axisymmetric wall temperature conditions in a vertical differentially heated cylinder. We show that the degree of asymmetry exhibited by the flow depends on the ratio between the amplitude of the maximum azimuthal and vertical temperature difference and on the ratio between the maximum calculated fluid velocity magnitude and "thermal diffusion" speed (thermal Peclet number).

The object of this work was to develop and implement a numerical method capable of solving the non-linear partial differential equations governing heat, mass and momentum transfer in a 3D cylindrical geometry in order to examine the character of convection in an asymmetrically heated cylindrical ampoule. The details of the numerical method, including verification tests involving comparison with results obtained from other methods, is given in Appendix 1. The results<sup>1</sup> of our study of 3D convection in an asymmetrically heated cylinder is described in the following sections.

## 2. INTRODUCTION AND BACKGROUND

The character of convection during solidification has been examined using numerical models of buoyancy-driven convection in cylindrical and rectangular geometries [1-12]. Early work [1-3] includes a variety of imposed temperature boundary conditions. These range from purely vertical temperature gradients which results in convection after a critical value of the Rayleigh number is exceeded [4], to idealized conditions associated with Bridgman-Stockbarger furnaces [3] which are imposed directly on the melt and crystal without consideration of the heat transfer between the ampoule, furnace and sample. For these boundary conditions, flow always occurs owing to the presence of radial temperature gradients. Later models [5,6] have accounted for the presence of the ampoule, and the details of furnace design. In an actual growth situation the thermal profile of the inner surface of the furnace is not realized at the ampoule wall; it is modified by heat transfer between the crystal, melt, ampoule and the furnace itself. The tendency is to reduce axial temperature gradients, while radial temperature gradients may increase or decrease

---

<sup>1</sup>These results are contained in paper submitted to the Physics of Fluids A.

depending on the specific nature of the heat transfer between the charge and ampoule [5]. The influence of melt convection on dopant distribution has been examined for dilute and non-dilute melts [3,5,9]. For a given furnace-ampoule combination the amount of compositional non-uniformity (or radial segregation) was shown to be a non-linear function of the Rayleigh number "Ra". The growth rate and physical properties of the melt also influence the degree of compositional uniformity in the grown crystal. These studies were restricted to cases for which the thermal boundary conditions possessed azimuthal symmetry.

Recently, non-axisymmetric convection has been observed in directional solidification experiments conducted with low melting point, low thermal conductivity materials [13,14]. The observed flows were explained by lack of azimuthal symmetry in the temperature field caused by the fact that the particular Bridgman-Stockbarger solidification apparatus precluded any control of the azimuthal temperature field. Indeed, such a situation may be common in many instances where the Bridgman-Stockbarger technique is employed owing to the difficulties involved with constructing an axisymmetric heating arrangement and in aligning the ampoule axis with the axis of the furnace. During growth of high temperature materials, any misalignment of the ampoule will result in an azimuthal variation in the radiation view factors for the ampoule. This will lead to asymmetry in the temperature of the ampoule wall.

The object of this work is to examine the character of convection in an asymmetrically heated cylindrical ampoule. In section 3 we formulate the model problem. In section 4 we outline the pseudo-spectral collocation method used to solve the 3D problem. The results are presented in section 5 and discussed in section 6.

### 3. FORMULATION OF THE PROBLEM

A practically desirable Bridgman-Stockbarger set-up such as that described by Dahkoul et al. [15] consists of three distinct thermal zones. The simplest arrangement has a hot zone (in which, ideally, the temperature at the wall and in the melt should be almost isothermal) and a cold zone. These are separated by a gradient zone in which a thermal barrier controls the heat transfer between the ampoule and the hot and cold zones. The basic Bridgman-Stockbarger model used here is shown in Fig.1. The fluid is differentially heated in a vertical cylinder having a length  $2H$  and a diameter  $D$ . The lower and upper endwalls of the cylinder are maintained at constant temperatures  $T_M$  and  $T_H$  respectively (where  $T_M < T_H$ ). In this system the presence of the thermal barrier is approximated by taking the cylinder walls to be adiabatic in the region corresponding to the gradient zone. In the hot zone we impose asymmetry in the temperature distribution using a function which causes

azimuthal and vertical deviations from isothermal conditions on the cylinder wall. The maximum lateral deviation in temperature is given by  $\Delta T_0$  (see Fig. 1). All boundaries of the cylinder are rigid with no-slip conditions for the velocities.

The equations governing energy, momentum and mass transport are written in primitive variables for cylindrical coordinates and using the Boussinesq approximation. They are rendered dimensionless using  $L^*$ ,  $V^*$ ,  $L^*/V^*$  and  $T_H - T_M$  as characteristic scales for length, velocity, time and temperature, respectively. The dimensionless equations are:

$$\frac{\partial T}{\partial t} = \frac{\Delta T}{Re \, Pr} - \mathbf{V} \cdot \text{grad } T, \quad (1)$$

$$\frac{\partial \mathbf{V}}{\partial t} = \frac{\Delta \mathbf{V}}{Re} - (\text{grad } \mathbf{V}) \cdot \mathbf{V} - \text{grad } p + \frac{Ra}{Pr \, Re^2} T \mathbf{k}, \quad (2)$$

$$\text{div } \mathbf{V} = 0, \quad (3)$$

where  $t$  is the time and  $\mathbf{V} = (v_r, v_\theta, v_z)$ ,  $p$  and  $T = \frac{(\bar{T} - T_M)}{(T_H - T_M)}$  respectively represent the dimensionless velocity, pressure and temperature. The unit vector in the  $z$ -direction is denoted by  $\mathbf{k}$ ,  $Pr = \frac{\nu}{\kappa}$  is the Prandtl number, with  $\nu$  the kinematic viscosity and  $\kappa$  the thermal diffusivity,  $Ra = \frac{g\alpha(L^*)^3(T_H - T_M)}{\kappa\nu}$  is the Rayleigh number, with  $g$  the gravitational acceleration, and  $\alpha$  the thermal expansion coefficient, and  $Re = \frac{L^*V^*}{\nu}$  is the Reynolds number.

Several choices are possible for these characteristic scales. In our computations, after trying several kinds of scaling, the choice  $V^* = \frac{\nu Ra}{L^* Pr}$  (i.e.  $Re = \frac{Ra}{Pr}$  = Grashof number) proved to be the best for obtaining good convergence behavior. This scaling has been suggested by Ostrach [16]. For the choice of  $L^*$ , the length  $H$  proved to be more convenient for computational purposes, primarily because of the chosen numerical method (see section 3). By exploring the different scalings, we have noted that the convergence behavior of the numerical method described in section 3, could be changed significantly (for the worse) when the parameters multiplying diffusive terms (Laplacians) are too small or too large. These considerations led us to recast equations (1) and (2) in the form

$$\frac{\partial T}{\partial t} = \frac{1}{Pr} \Delta T - \frac{Ra}{Pr} \mathbf{V} \cdot \text{grad } T, \quad (4)$$

$$\frac{\partial \mathbf{V}}{\partial t} = \Delta \mathbf{V} - \frac{Ra}{Pr} (\text{grad } \mathbf{V}) \cdot \mathbf{V} - \text{grad } p + T \mathbf{k}. \quad (5)$$

Finally equations (3-5) are solved as functions of the independent variables  $(r, \theta, z)$  in the domain  $\Omega = ] 0, \frac{1}{A} [ \times ] 0, 2\pi [ \times ] -1, 1 [$ . Here the aspect ratio  $A$  is defined as  $2H/D$ , where  $D$  is the diameter.

The following conditions were applied at the initial iterate ( $t \leq 0$ )

$$v_r = v_\theta = v_z = 0, \quad (6a)$$

$$T = g(r, \theta, z) f(z), \quad (6b)$$

with 
$$f(z) = \frac{1}{1 - \exp(\sigma)} \left[ \exp\left(\frac{\sigma(1-z)}{2}\right) - \exp(\sigma) \right]$$

and 
$$g(r, \theta, z) = 1 + A_0 \frac{1-z}{3} \exp\left(\frac{-2z-1}{4}\right) (\cos(\pi-\theta)-1) \sin^2\left(\frac{r\pi A}{2}\right).$$

In order to avoid discontinuities in derivatives of the temperature, the abrupt transition between the hot zone and the adiabatic zone the function  $f(z; \sigma)$  is used. The parameter  $\sigma$  is chosen such that were it not for the azimuthal temperature perturbation, the dimensionless wall temperature due to  $f(z; \sigma)$  would be almost equal to 1 for  $z > Z_a$ , where  $Z_a$  is the  $z$ -coordinate of the location of the upper limit of the adiabatic zone. The function  $g(r, \theta, z)$  gives the initial condition for the azimuthal variation in temperature. The maximum azimuthal temperature deviation is denoted by  $\Delta T_\theta$ . It is convenient to express this deviation as a percentage of the axial temperature difference  $T_H - T_M$ ; i.e.  $A_\theta = \frac{\Delta T_\theta \times 100\%}{T_H - T_M}$ .

Table 1 gives  $A_\theta$  ( $A_\theta = 2 A_0 \left(\frac{1-Z_a}{3}\right) \exp\left(\frac{-2Z_a-1}{4}\right)$ ) for different values of  $A_0$  and different aspect ratios.

The following dimensionless boundary conditions are applied at  $t > 0$

$$v_r = v_\theta = v_z = 0 \text{ at } z = \pm 1 \text{ and } r = \frac{1}{A}, \quad (7a)$$

$$T = 0 \text{ at } z = -1, \quad T = 1 \text{ at } z = 1, \quad (7b)$$

$$T = g(r, \theta, z) f(z) \text{ at } r = \frac{1}{A} \text{ and } z > Z_a \text{ (} z \neq \pm 1 \text{)} \quad (7c)$$

$$\frac{\partial T}{\partial r} = 0 \text{ at } r = \frac{1}{A} \text{ and } z \leq Z_a, \quad (7d)$$

The azimuthal temperature variation on the ampoule wall is given by  $g(\frac{1}{A}, \theta, z)$  and is enforced only for the hot zone  $z > Z_a$ .

Table 1. Values of the percentage of azimuthal temperature difference  $A_\theta$

Aspect Ratio	$A_0$	$A_\theta$
1	0.1	10%
1	0.02	2%
1	0.2	20%
2	0.1	13.2%
2	0.2	26.4%

#### 4. NUMERICAL METHOD

The equations (3-5) have been solved using a modified version of the Fourier-Chebyshev pseudospectral method introduced by Pulicani and Ouazzani [17]. For this method the singularity which arises at  $r=0$  when using cylindrical coordinates (without axisymmetry) [18] is avoided by using a change of dependent variables. The singularity arises because  $r=0$  is an artificial boundary of the computational domain; i.e. it occurs only by construction of the coordinate system. The change of variables used to cope with the singularity is

$$T = \frac{\tilde{T}}{r}, \quad v_r = \frac{\tilde{v}_r}{r}, \quad v_\theta = \frac{\tilde{v}_\theta}{r}, \quad v_z = \frac{\tilde{v}_z}{r} \quad \text{and} \quad p = \frac{\tilde{p}}{r}. \quad (8)$$

Application of (3-8) yields a system of equations with  $\tilde{T}$ ,  $\tilde{v}_r$ ,  $\tilde{v}_z$ ,  $\tilde{p}$  and  $\tilde{v}_\theta$ , as unknowns. Obviously,  $\tilde{T} = \tilde{v}_r = \tilde{v}_z = \tilde{v}_\theta = \tilde{p} = 0$  at  $r = 0$ . These equations are then discretized with respect to time,  $t = n \delta t$ , by means of a second order semi-implicit scheme. The latter employs a combination of the Adams-Bashforth and Crank-Nicolson schemes, namely

$$\left(r - \frac{r}{2} \frac{\delta t}{Pr} \Delta\right) \left(\frac{\tilde{T}^{n+1} - \tilde{T}^n}{r}\right) = \tilde{F}^{n,n-1}, \quad (9)$$

$$\left(r - \frac{r}{2} \frac{\delta t}{Pr} \Delta\right) \left(\frac{\tilde{V}^{n+1} - \tilde{V}^n}{r}\right) = \tilde{G}^{n,n-1,n+1} - \delta t r \left[\text{grad} \frac{\tilde{p}}{r}\right]^{n+1}, \quad (10)$$

$$\left(\text{div} \frac{\tilde{V}}{r}\right)^{n+1} = 0, \quad (11)$$

with

$$\tilde{F}^{n,n-1} = \delta t \left[ \frac{r}{Pr} \Delta \left(\frac{\tilde{T}}{r}\right) - \frac{3 Ra}{2 Pr} \tilde{V} \cdot \text{grad} \left(\frac{\tilde{T}}{r}\right) \right]^n + \frac{\delta t Ra}{2 Pr} \left[ \tilde{V} \cdot \text{grad} \left(\frac{\tilde{T}}{r}\right) \right]^{n-1},$$

and

$$\tilde{G}^{n,n-1,n+1} = \delta t \left[ r \Delta \left(\frac{\tilde{V}}{r}\right) - \frac{3 Ra}{2 Pr} \left(\text{grad} \frac{\tilde{V}}{r}\right) \cdot \tilde{V} \right]^n + \frac{\delta t Ra}{2 Pr} \left[ \left(\text{grad} \frac{\tilde{V}}{r}\right) \cdot \tilde{V} \right]^{n-1} + [\tilde{T} \mathbf{k}]^{n+1},$$

where for convenience we have defined  $\tilde{V} = (\tilde{v}_r, \tilde{v}_\theta, \tilde{v}_z)$ .

With this method [17], problems encountered with satisfying (11) are surmounted by using artificial compressibility [19,20]. A false timestep is employed and the method is only applicable for steady solutions to the system (3-7). Because of the stiffness of the physical problem at low Prandtl numbers, obtaining rapid convergence with this method at high Rayleigh numbers is difficult. In order to overcome this problem, we have modified the method by introducing two iterative processes. An outer iteration which is related to each timestep and an inner iteration which ensures that (11) is satisfied to some  $\epsilon \ll 0$  for each outer iterative step. It is clear that for lower values of  $\epsilon$ , this pseudo-unsteady method takes on the character of an unsteady calculation. For this reason we have used an Adams-Bashforth scheme to discretize the convective terms instead of simply taking them explicitly [17] at the instant  $t = n \delta t$  in  $\tilde{F}^{n,n-1}$  and  $\tilde{G}^{n,n-1,n+1}$ .

A generalized ADI procedure [19] is then applied to reduce the problem to the successive solution of one-dimensional problems. For clarity, we present the method only as applied to the momentum transport equation. It is readily extended to cope with the energy transport equation. At each time step the following problem is solved

$$\left(1 - \frac{\delta t}{2} \Lambda_\theta\right) \mathbf{V}^* = \tilde{G}^{n,n-1,n+1} - \delta t r \left[\text{grad} \frac{\tilde{p}}{r}\right]^{n+1,\mu}, \quad (12a)$$



$$\left(1 - \frac{\delta t}{2} \Lambda_z\right) \mathbf{V}^{**} = \mathbf{V}^*, \quad (12b)$$

$$\left(r - \frac{r \delta t}{2} \Lambda_r\right) (r^{-1} \mathbf{V}^{**}) = \mathbf{V}^{**}, \quad (12c)$$

$$\tilde{\mathbf{V}}^{n+1, \mu+1} = \tilde{\mathbf{V}}^n + \mathbf{V}^{***}, \quad (12d)$$

$$\tilde{p}^{n+1, \mu+1} = \tilde{p}^{n+1, \mu} - \lambda r \left( \operatorname{div} \frac{\tilde{\mathbf{V}}}{r} \right)^{n+1, \mu+1}, \quad (12e)$$

where  $\lambda$  is a strictly positive constant and  $\mu$  ( $\mu = 0, 1, \dots, N_\mu$ ) is the superscript connected to the inner iterative process. The operator  $\Delta$  occurring in (10) has been decomposed so that  $\Delta = \Lambda_r + \Lambda_\theta + \Lambda_z$ . Here the  $\Lambda_\alpha$ , are related to the independent variables  $r$ ,  $\theta$  and  $z$ , respectively. Note that for  $\mu = 0$ ,  $\left[ \operatorname{grad} \frac{\tilde{p}}{r} \right]^{n+1, 0} = \left[ \operatorname{grad} \frac{\tilde{p}}{r} \right]^n$ . Equation (12e) has no physical meaning until  $\delta \tilde{p}^{n+1} = \tilde{p}^{n+1, \mu+1} - \tilde{p}^{n+1, \mu} = 0$  (or practically speaking, is sufficiently small). If  $\delta \tilde{p}^{n+1}$  is identically zero at each time step the method is no longer pseudo-unsteady. The present way to deal with the pressure can be time consuming when the number of internal iterations  $N_\mu$  is too high. However, since we seek steady solutions, the iterative process has been introduced only to help the convergence when the solution is very stiff. It is stopped as soon as the divergence of the velocity reaches a certain value  $\epsilon$ . The maximum value of  $N_\mu$  is chosen such that the convergence is obtained after a reasonable number of outer iterations, but not so high that the divergence of the velocity is  $\epsilon$  at the beginning of the outer iteration. The optimum values of  $N_\mu$  and  $\epsilon$  will be defined in the next section. A standard Fourier-Galerkin approximation [18] is employed for the solution of (12a).

The most convenient (see section 2) choice of characteristic length is  $L^* = H$ . This leads directly to the domain  $-1 \leq z \leq 1$  which is required for the Chebyshev-collocation method [20] used to solve equations (12b) and (12c). The boundary conditions are introduced by replacing the right hand sides of (12b) and (12c) by the appropriate terms [17].

The energy equation is solved in the same manner as the momentum transport equations but, obviously, needs no inner iterations to satisfy the divergence equation. The solution algorithm takes the following steps :

- (i) With  $\tilde{T}^n$ ,  $\tilde{T}^{n-1}$ ,  $\tilde{V}^n$  and  $\tilde{V}^{n-1}$  known, we deduce  $\tilde{F}^{n, n-1}$  and then  $\tilde{T}^{n+1}$ .
- (ii) Using  $\tilde{T}^{n+1}$ ,  $\tilde{V}^n$  and  $\tilde{V}^{n-1}$ , we calculate  $\tilde{G}^{n, n-1, n+1}$  and then, finally,  $\tilde{V}^{n+1}$  and  $\tilde{p}^{n+1}$  with (12).

In all of the results we present here the above method requires a distribution of points such that

$$\theta_k = \frac{2\pi k}{N_\theta}, \quad k = 0, \dots, N_\theta - 1, \quad (13a)$$

$$z_j = \cos\left(\frac{\pi j}{N_z - 1}\right), \quad j = 0, \dots, N_z - 1, \quad (13b)$$

$$r_i = \frac{1}{2A} \left[ \cos\left(\frac{\pi i}{N_r - 1}\right) + 1 \right], \quad i = 0, \dots, N_r - 1, \quad (13c)$$

with  $N_r$ ,  $N_\theta$  and  $N_z$  the number of collocation points between  $r = 0$  and  $1/A$ ,  $\theta = 0$  and  $2\pi$ , and  $z = -1$  and  $1$ , respectively.

In our discussion of the results we shall also refer to the residual of  $\vartheta$ , denoted  $R_\vartheta$ , which is calculated on the collocation points of  $\vartheta = \{T, v_r, v_\theta, v_z\}$ . Furthermore,

$$R_\vartheta = \text{Max}_{i,k,j} \left[ \frac{|\vartheta(r_i, \theta_k, z_j)^{n+1} - \vartheta(r_i, \theta_k, z_j)^n|}{\delta t \vartheta(r_i, \theta_k, z_j)^{n+1}} \right], \quad (14)$$

with  $i = 0, \dots, N_r - 1$ ,  $k = 0, \dots, N_\theta - 1$ ,  $j = 0, \dots, N_z - 1$ .

We denote the maximum values of  $v_r$ ,  $v_\theta$ ,  $v_z$ ,  $v_x$  and  $v_y$  by  $v_{r \max}$ ,  $v_{\theta \max}$ ,  $v_{z \max}$ ,  $v_{x \max}$  and  $v_{y \max}$ , respectively. The variables  $v_x$  and  $v_y$  are the velocities in Cartesian coordinates such that  $v_x = v_r \cos \theta - v_\theta \sin \theta$ , and  $v_y = v_r \sin \theta + v_\theta \cos \theta$ . As these maxima are calculated at the collocation points particular to each method, small differences are expected in the results.

For all the results presented in the following section the starting condition (6b) has only been used for  $Ra = 10$ . For the others, the starting condition was the solution calculated with a lower  $Ra$ . The adiabatic zone covers one fourth of the cylinder's height when the aspect ratio  $A = 1$  (i.e.  $Z_a = -0.5$ ) and one eighth when  $A = 2$  (i.e.  $Z_a = -0.75$ ). The calculations have been performed on a Cray XMP computer by using a spatial resolution such that  $N_r \times N_\theta \times N_z = 13 \times 20 \times 31$  when  $A = 1$  and  $N_r \times N_\theta \times N_z = 13 \times 20 \times 61$  when  $A = 2$ . For all calculations the parameter  $\lambda$  (see (12e)) is equal to 1.3,  $20 < N_\mu < 30$ , and the time-step  $\delta t$  chosen between  $1 \cdot 10^{-4}$  and  $1 \cdot 10^{-5}$  according to the stiffness of the solution. Note that we have stopped our calculations when the divergence  $\text{div } \mathbf{V} \approx 10^{-8}$  and  $\text{ResV} \approx 10^{-4}$ . No significant change in the values of the velocity and temperature fields if  $\text{divV}$  and  $\text{ResV}$  are decreased further. For the problem described here a comparison has been made between our method and the finite element code FIDAP

[21,22]. For FIDAP an irregularly spaced Cartesian grid with nodes  $N_x \times N_y \times N_z = (9 \times 11 \times 31)$  was employed (see Fig. 2).

For the purposes of presenting the results we define two dimensionless measures of the velocity, a Reynolds number  $Re_{*max} = Re_{*max} = \bar{v}_{*max} D / \nu$  and a thermal Peclet number  $Pe_{*max} = \bar{v}_{*max} D / \kappa$ , where a "\*" corresponds to the coordinate directions (i.e. r, z, q, x, or y). The thermal Peclet number represents a ratio of the magnitudes of the maximum dimensional convective velocity and a thermal diffusion velocity.

## 5. RESULTS

Table 2 shows the results of a comparison between our method and the finite element code FIDAP [21,22]. The values of  $Re_{x max}$ ,  $Re_{y max}$  and  $Re_{z max}$ , were obtained with  $Ra = 250, 2500$  and  $1500$ . Clearly, there is good agreement between these two methods for  $Ra$  between 250 and 2500, while for  $Ra=15000$ , the poor agreement is only due to the smaller number of points in the z-direction employed for FIDAP.

Table 2. Comparison between results obtained from the Spectral method and from FIDAP

	SPECTRAL			FIDAP		
Ra	$Re_{x max}$	$Re_{y max}$	$Re_{z max}$	$Re_{x max}$	$Re_{y max}$	$Re_{z max}$
250	10	7	20	12	8	21
2500	60	61	103	067	069	104
15000	263	192	286	295	216	386

Table 3 summarizes the details of our computations for  $A = 1, 2$ ,  $2500 \leq Ra \leq 64000$  and  $2\% < A_\theta < 27\%$ . A comparison of the velocity fields in the  $\theta = 0^\circ$  and  $180^\circ$  sections for  $A_\theta = 2\%$  and  $Ra=2500$ , and  $Ra = 24,000$  is given in Fig. 3. The flow is barely perceptible at the lower  $Ra$ . Comparison of Fig. 3 with Fig. 4., which shows the velocity fields for  $Ra = 2500, 15000$  and  $24000$ , reveals the effect of increasing the temperature asymmetry. The effect of increasing  $Ra$  at fixed  $A_\theta$  is also seen in Fig. 4. Note that the locations of the roll centers change as  $Ra$  is increased. Figure 5. depicts the velocity and temperature fields for three vertical sections at  $Ra = 15,000$  for  $A_\theta = 20\%$ . Horizontal sections of the velocity field for the  $Ra=15,000$  case are shown in Fig. 6.

The effect of increasing the aspect ratio is seen upon comparison of Fig. 4 with Fig. 7 which has been calculated for  $Ra = 2500$  and  $15000$  with  $A_0 = 0.2$  ( $A_\theta = 26.4\%$ ). The basic asymmetry of the flow is not affected significantly by the increase in aspect ratio,

although the centers of the toroidal rolls are shifted. Horizontal sections of the flow shown in Fig. 6 are depicted in Fig. 7.

Table 3. Summary of the results for  $Pr = 10^{-2}$

Ra	A	$A_0$	$\delta t$	$Re_{r \max}$	$Re_{\theta \max}$	$Re_{z \max}$
2500	1	0	$10^{-4}$	70	0	122
	1	0.02	$10^{-4}$	69	7	120
	1	0.2	$10^{-4}$	61	56	103
	2	0.1	$10^{-5}$	69	44	114
	2	0.2	$10^{-5}$	69	59	125
6400	1	0.2	$10^{-4}$	112	123	168
	2	0.1	$10^{-4}$	128	99	191
15000	1	0	$10^{-4}$	205	0	314
	1	0.02	$10^{-4}$	222	42	307
	1	0.2	$10^{-4}$	220	254	286
	2	0.1	$10^{-5}$	209	175	294
	2	0.2	$10^{-5}$	188	228	425
24000	1	0	$10^{-4}$	242	0	384
	1	0.02	$10^{-4}$	267	62	376
	1	0.2	$7 \times 10^{-5}$	318	363	373
64000	1	0	$10^{-4}$	338	0	583

Comparison of Figs. 8 and 9 for  $Ra = 15000$  and  $A_0 = 13.2\%$  with Figs. 10 and 11 for  $Ra=2500$ ,  $A_0 = 13.2\%$ , reveals that in the higher Rayleigh number case two additional cells have formed in the upper half of the cylinder. These are barely detectable in the  $Ra=2500$  case. At higher values of  $A_0$  these cells are able to develop well for lower values of  $Ra$ . In Fig. 7 the twofold increase in  $A_0$  leads to well developed upper cells even at  $Ra = 2500$ .

Figs. 12 and 13. depict the results obtained for  $Pr = 1$ ,  $Ra = Gr = 2.5 \times 10^5$ . Comparison of these results with Figs. 8 and 9 ( $Pr = 10^{-2}$ ,  $Ra = 2500$ ,  $Gr = 2.5 \times 10^5$ ) reveals the effect of increasing  $Pr$  while holding the Grashof number fixed. There is a decrease in the degree of asymmetry in the flow for the lower Prandtl number case. The cylinder is dominated by a large asymmetric roll which extends along most of the cylinder with smaller secondary roll along the bottom of the cylinder. The isotherms which extend into the adiabatic zone have been modified by the flow and are considerably flatter than their low  $Pr$  counterparts.

## 6. DISCUSSION AND SUMMARY

The results of an experimental investigation into the nature of asymmetric flow during Bridgman-Stockbarger directional solidification of Salol by Neugebauer and Wilcox [14] led to the conclusion that the degree of flow asymmetry decreases with increasing convective flow velocities. Furthermore they conjectured that for the same experimental conditions, low Prandtl number fluids to exhibit correspondingly less asymmetry owing to the more rapid flow velocities which would necessarily ensue. It can be discerned from the results presented in section 4 that our calculations predict that for a fixed value of  $A_0$  and  $Pr$  an increase in  $Re_{*max}$  (in practical terms caused by an increase in  $\Delta T = T_H - T_M$ ) tends to amplify the asymmetry. Examination of the experimental results of [14] reveals that when  $\Delta T$  was increased,  $\Delta T_\theta$ , the azimuthal variation in temperature, remained the same. In other words, the relative temperature asymmetry  $A_\theta$  was decreased. Thus, the observed decrease in flow asymmetry can be explained merely by the fact that the azimuthal temperature variation was less significant for the higher  $Ra$  cases. This trend is confirmed by our calculations.

Our calculations do confirm the prediction made in [14] that, for otherwise equivalent conditions, the higher  $Pr$  case will exhibit more asymmetry in the flow than the low  $Pr$  case. That the flow asymmetry is reduced due to an increase in flow velocity (Reynolds number) contradicts our results presented in Table 3 and Figs. 4-9. The reduction in asymmetry can be explained, however, upon examination of relationship between the degree of flow asymmetry and the thermal Peclet number. The latter scale represents a thermal velocity magnitude. Table 4 clearly shows that at a fixed  $A_\theta$  there is an increase in the degree of flow asymmetry as the thermal Peclet number increases.

Table 4. Comparison of Peclet numbers for the  $Pr = 10^{-2}$  and  $Pr = 1$  cases.

Pr	$Pe_{r \max}$	$Pe_{\theta \max}$	$Pe_{z \max}$
$10^{-2}$	0.69	0.44	1.14
1	11.02	8.92	22.83

In summary, we have examined the consequences of azimuthal asymmetry in ampoule wall temperature in a differentially heated cylindrical ampoule containing an incompressible Newtonian fluid. The study was motivated by recent observations of non-axisymmetric convection in directional solidification experiments conducted with low melting point, low thermal conductivity materials [13,14]. Our results indicate that for a fixed value of the relative asymmetry in temperature  $A_{\theta}$ , the degree of asymmetry in the flow is accentuated as the thermal Peclet number is increased. For fixed  $Pr$  and  $Ra$ , the flow asymmetry increases if  $A_{\theta}$  is increased.

## 7. REFERENCES

- [1] P. A. Clark and W. R. Wilcox, *J. Crystal Growth* **50**, 461 (1980).
- [2] N. Kobayashi and W. R. Wilcox, *J. Crystal Growth* **59**, 616 (1982).
- [3] C. J. Chang, R. A. Brown, *J. Crystal Growth* **63**, 353 (1983).
- [4] G. B. McFadden, R. G. Rehm, S. R. Coriell, W. Clark and K. A. Morrish, *Metall. Trans.* **A15**, 2125 (1984).
- [5] P. M. Adornato, R. A. Brown, *J. Crystal Growth* **80**, 155 (1987).
- [6] D. H. Kim, P. M. Adornato and R. A. Brown, *J. Crystal Growth* **89**, 339 (1988).
- [7] V. I. Polezhaev, A. P. Lebedev, S. A. Nikitin, Proc. 5th European Symposium on Materials Sciences under Microgravity, Schloss Elmau FRG, ESA SP-222 237 (1984).
- [8] G. B. McFadden and S. R. Coriell, in Proc. AIAA/ASME/SIAM/APS 1st National Fluid Dynamics Congress, Cincinnati, July 25th-28th, 1572 (1988).
- [9] J. I. D. Alexander, J. Ouazzani and F. Rosenberger, *J. Crystal Growth* **97**, 285 (1989).
- [10] G. Müller, in Convective Transport and Instability Phenomena (eds. Zierp J. and Oertel H.) Braun Verlag, 441 (1982).
- [11] G. Müller, G. Neumann, and W. Weber, *J. Crystal Growth* **70**, 78 (1984).
- [12] G. Müller, "Convection and Inhomogeneities in Crystal Growth from the Melt," in *Crystals: Growth, Properties and Applications* **12**, Springer-Verlag, Berlin (1988).
- [13] H. Potts and W. R. Wilcox, *J. Crystal Growth* **73**, 350 (1985).
- [14] G. T. Neugebauer and W. R. Wilcox, *J. Crystal Growth* **89**, 143 (1988).
- [15] Y. M. Dahkoul, R. Farmer, S. L. Lehoczy and F. R. Szofran, *J. Crystal Growth* **86**, 49 (1988).

- [16] S. Ostrach, Ann. Rev. Fluid Mech. **14**, 313 (1982).
- [17] J.P. Pulicani and J. Ouazzani, A Fourier-Chebyshev Pseudospectral Method for Solving Steady 3-D Navier-Stokes and Heat Equations in Cylindrical Cavities, submitted to Computers and Fluids, (1990).
- [18] D. Gottlieb and S.A. Orszag, Numerical Analysis of Spectral Methods: Theory and Application, SIAM Monograph No. 26, SIAM, Philadelphia, U.S.A. (1977).
- [19] R. Peyret and T.D. Taylor, Computational Methods for Fluid Flow, Springer Verlag, New-York (1983).
- [20] J. Ouazzani and R. Peyret, Notes on Numerical Fluid Mechanics, (Edited by M. Pandolfi and R. Piva), 7, 275, Vieweg Verlag, Braunschweig (1984).
- [21] M.S. Engelman, FIDAP Fluid Dynamics Analysis Program Theoretical Manual, Fluid Dynamics International Inc., Revision 5 (1990).
- [22] M.S. Engelman and R.L. Sani, Proceedings of the ASME Convection in Enclosures Conference, ASME HTD 26 (1983).

## 8. FIGURE CAPTIONS

- Fig. 1 Model Bridgman-Stockbarger configuration.
- Fig. 2 Mesh used for the FIDAP calculations.
- Fig. 3 Comparison of the velocity fields in the  $\theta = 0^\circ$  and  $180^\circ$  sections and the  $(r, z)$  plane at  $z = 0$  with  $A_\theta = 2\%$  and  $Ra = 2500, 24000$ . Aspect ratio  $A = 1$  and  $Pr = 10^{-2}$ .
- Fig. 4 Comparison of the velocity fields in the  $\theta = 0^\circ$  and  $180^\circ$  section with  $A_\theta = 20\%$  and  $Ra = 2500, 15000$ , and  $24000$ . Aspect ratio  $A = 1$  and  $Pr = 10^{-2}$ .
- Fig. 5 Velocity and temperature fields with  $A_\theta = 20\%$  and  $Ra = 15000$  for  $\theta = 0^\circ$  and  $180^\circ$ ,  $54^\circ$  and  $234^\circ$ ,  $90^\circ$  and  $270^\circ$ . Aspect ratio  $A = 1$  and  $Pr = 10^{-2}$ .
- Fig. 6 Velocity field in the  $(r, \theta)$  plane with  $A_\theta = 20\%$  and  $Ra = 15000$  at  $z = 0.75, 0$ , and  $-0.75$ . Aspect ratio  $A = 1$  and  $Pr = 10^{-2}$ .
- Fig. 7 Velocity fields with  $A_\theta = 26.4\%$   $Ra = 2500$  and  $15000$  at  $\theta = 0^\circ$  and  $180^\circ$ ,  $54^\circ$  and  $234^\circ$ ,  $90^\circ$  and  $270^\circ$ . Aspect ratio  $A = 2$  and  $Pr = 10^{-2}$ .
- Fig. 8 Velocity and temperature fields with  $A_\theta = 13.2\%$  and  $Ra = 15000$  at  $\theta = 0^\circ$  and  $180^\circ$ ,  $54^\circ$  and  $234^\circ$ ,  $90^\circ$  and  $270^\circ$ . Aspect ratio  $A = 2$  and  $Pr = 10^{-2}$ .
- Fig. 9 Velocity field in the  $(r, \theta)$  plane with  $Ra = 15000$  at  $z = 0.5, 0, -0.5$ , and  $-0.87$ . Aspect ratio  $A = 2$  and  $Pr = 10^{-2}$ .
- Fig. 10 Velocity field with  $A_\theta = 13.2\%$  and  $Ra = 2500$  at  $\theta = 0^\circ$ ,  $54^\circ$ , and  $90^\circ$ . Aspect ratio  $A = 2$  and  $Pr = 10^{-2}$ .
- Fig. 11 Velocity field in the  $(r, \theta)$  plane with  $Ra = 2500$  at  $z = 0.5, 0, -0.5$ , and  $-0.87$ . Aspect ratio  $A = 2$  and  $Pr = 10^{-2}$ .
- Fig. 12 Velocity and temperature fields with  $A_\theta = 13.2\%$  and  $Ra = 250000$  at  $\theta = 0^\circ$  and  $180^\circ$ ,  $54^\circ$  and  $234^\circ$ ,  $90^\circ$  and  $270^\circ$ . Aspect ratio  $A = 2$  and  $Pr = 1$ .
- Fig. 13 Velocity field in the  $(r, \theta)$  plane with  $Ra = 250000$  at  $z = 0.5, 0, -0.5$ , and  $-0.87$ . Aspect ratio  $A = 2$  and  $Pr = 1$ .



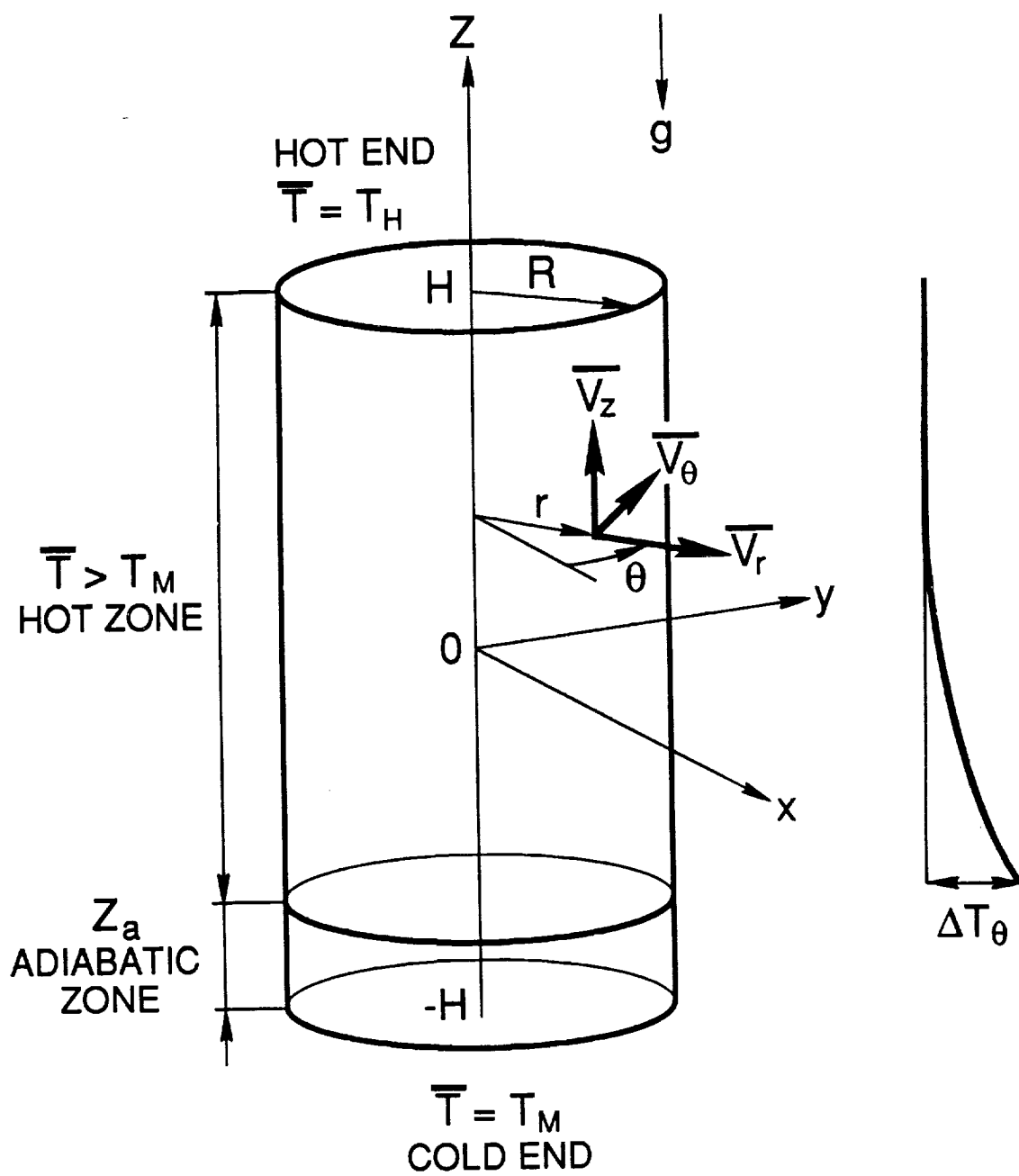


FIG. 1

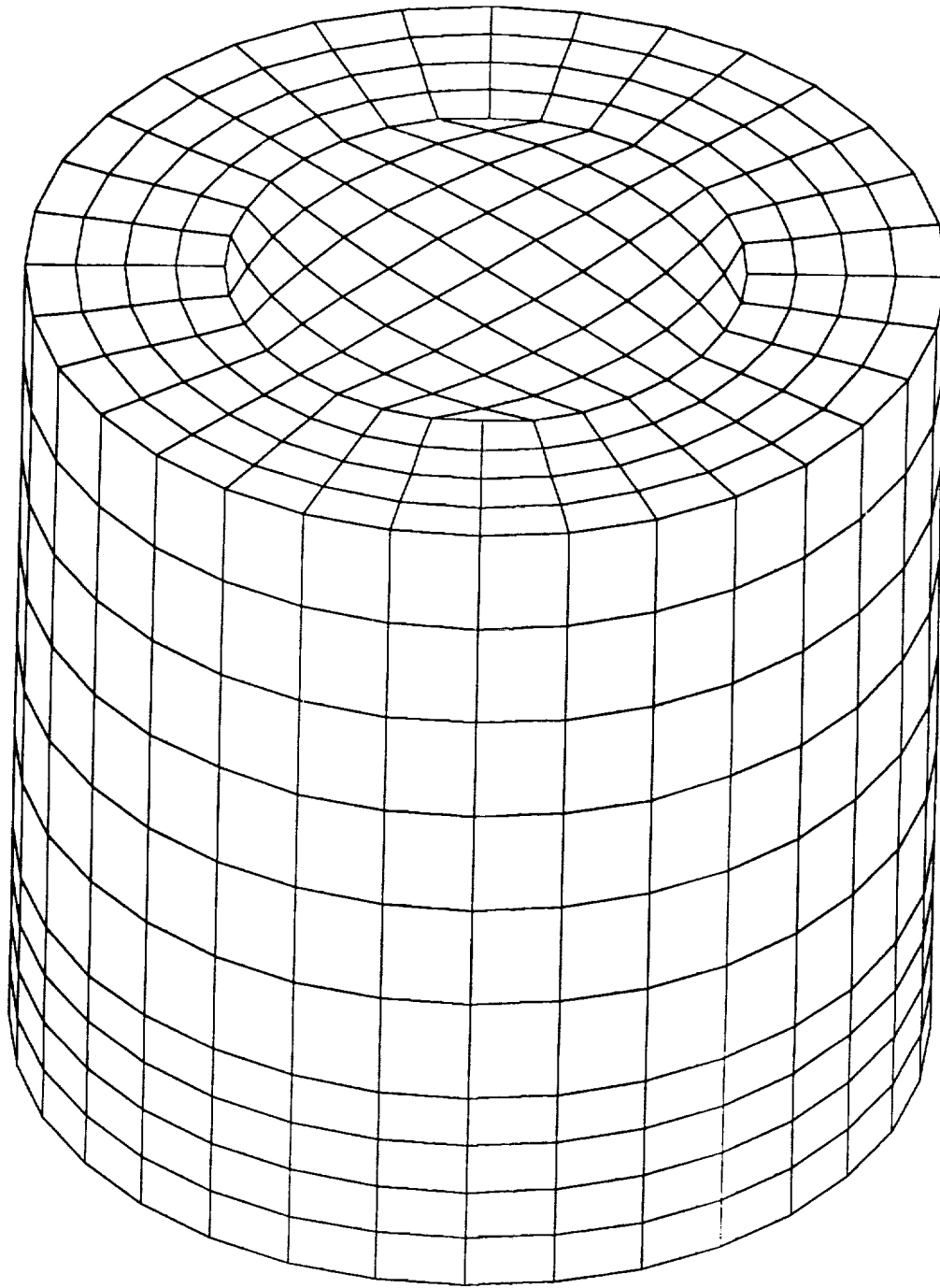
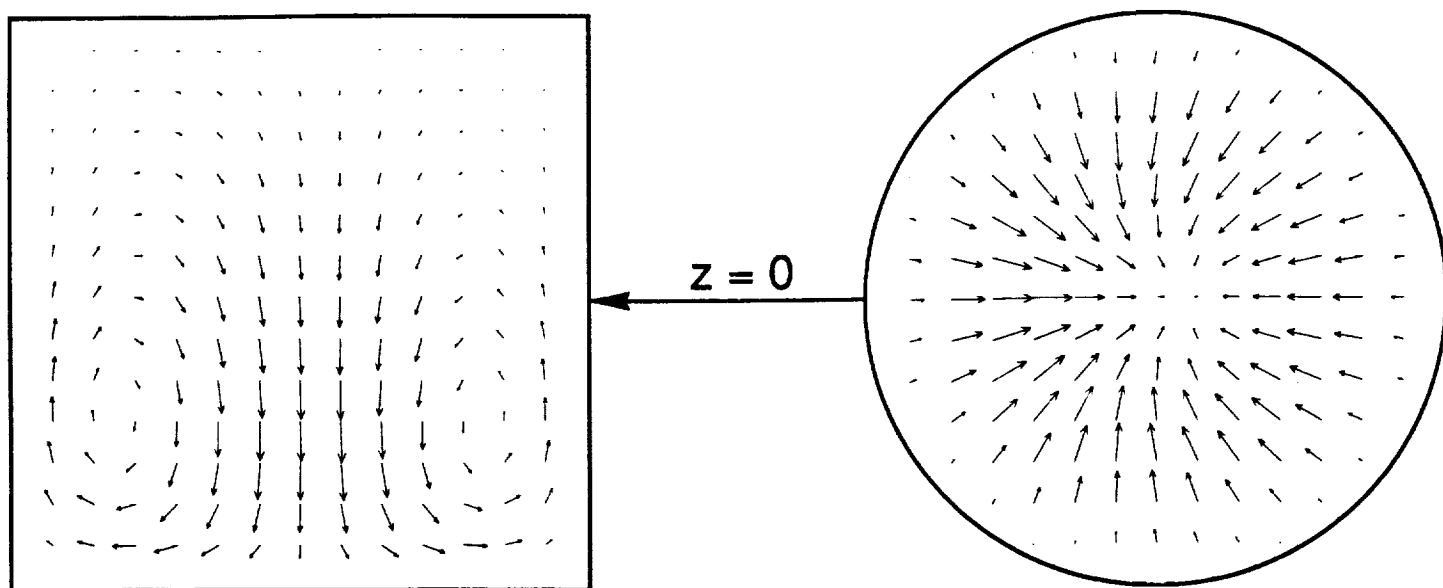
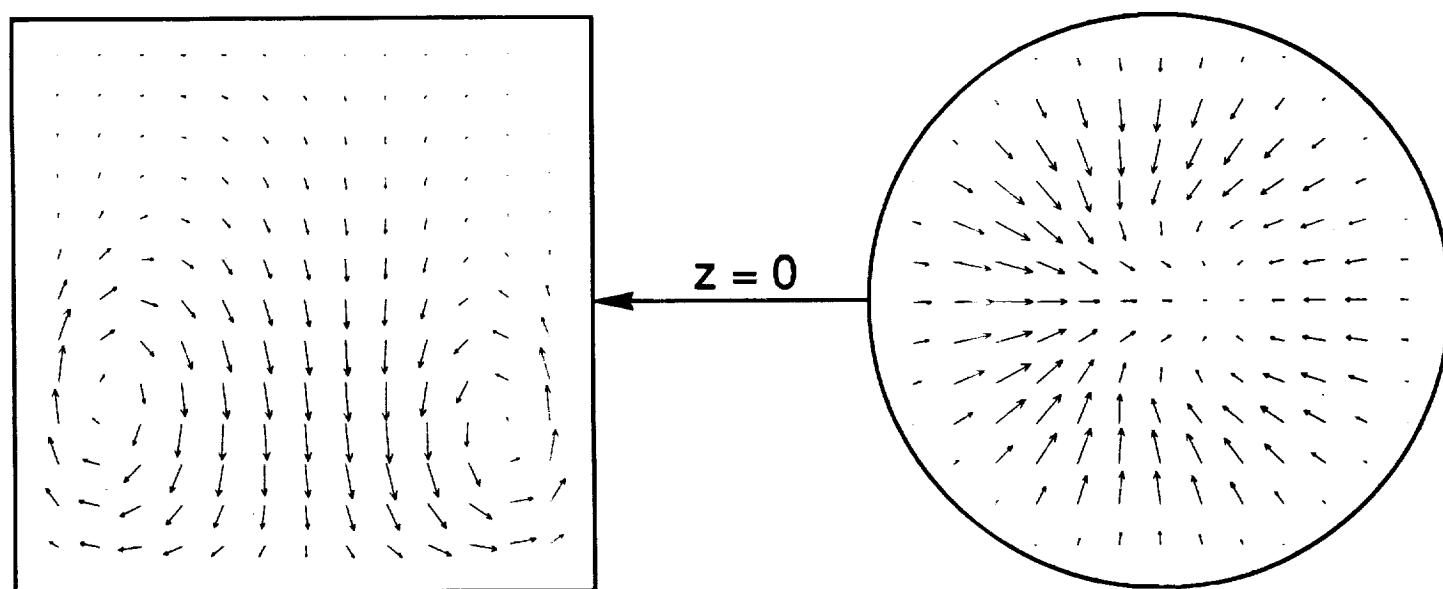


FIG. 2

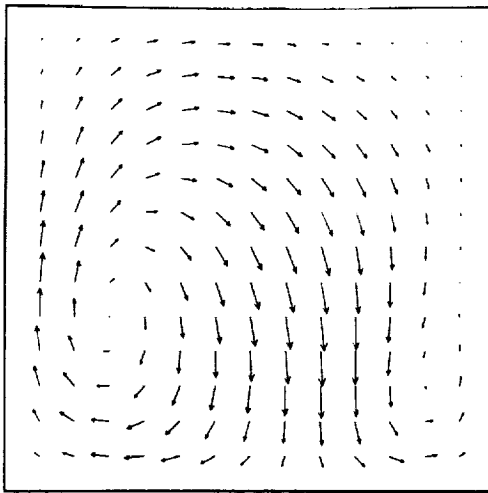


$Ra = 2500$

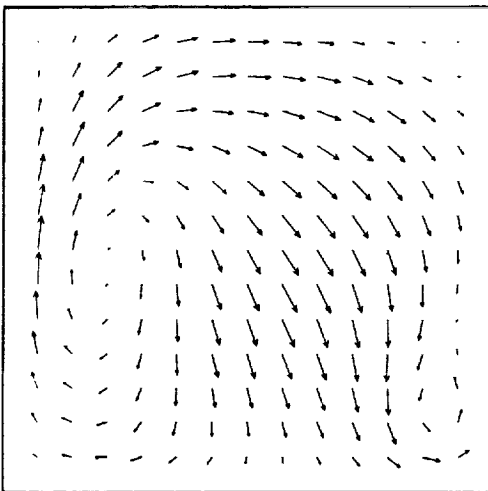


$Ra = 24000$

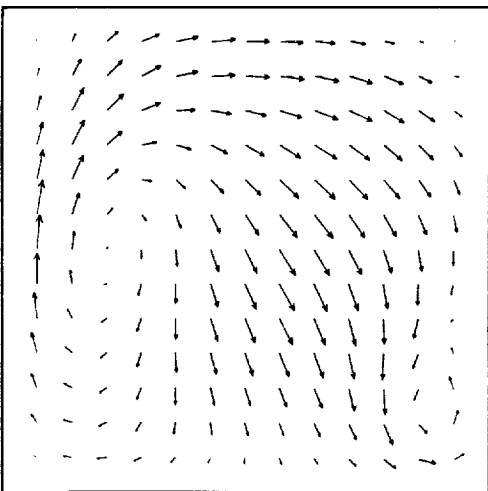
FIG. 3



$Ra = 2500$

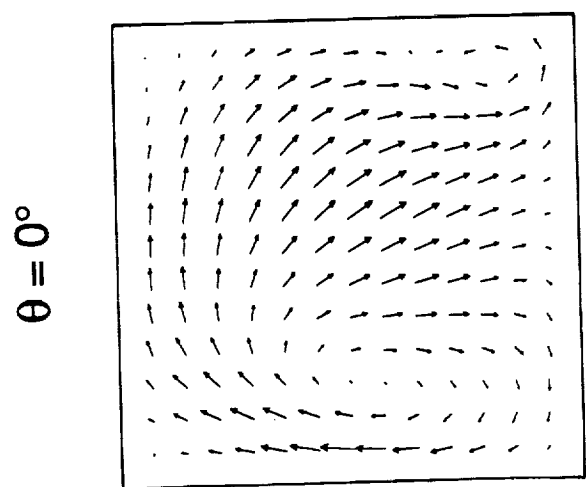
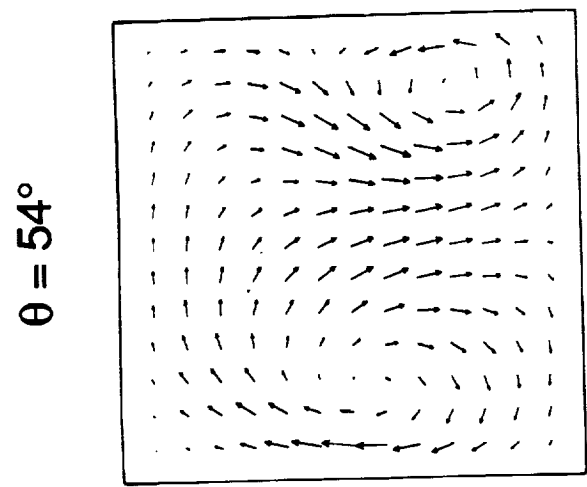
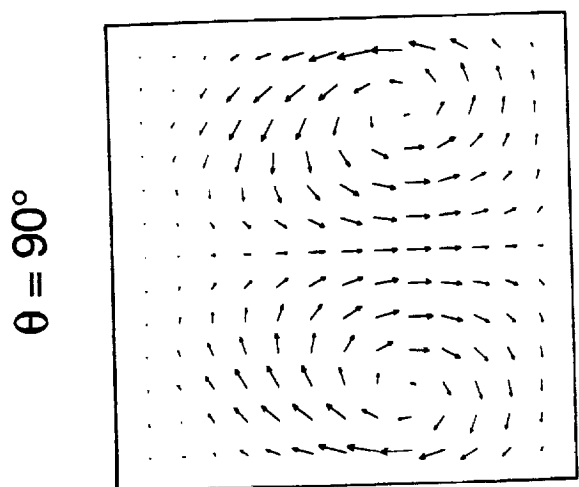


$Ra = 15000$

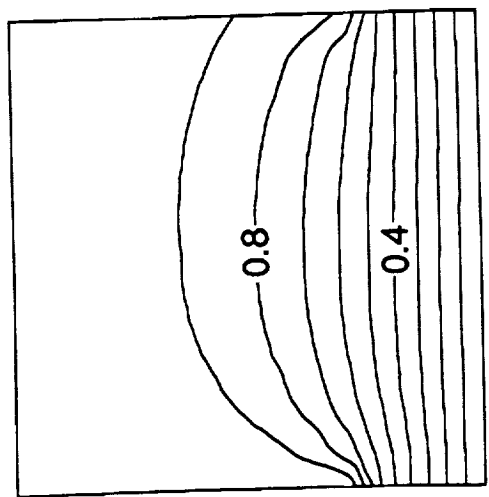
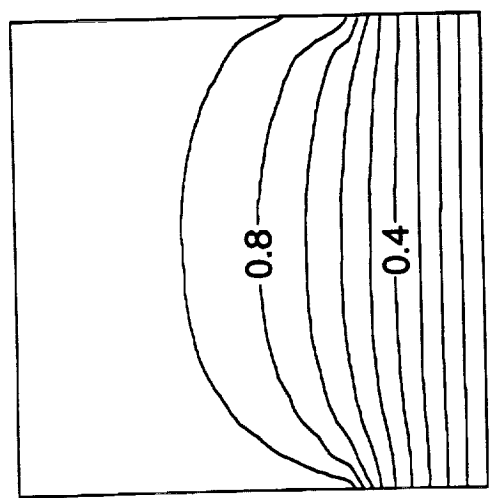
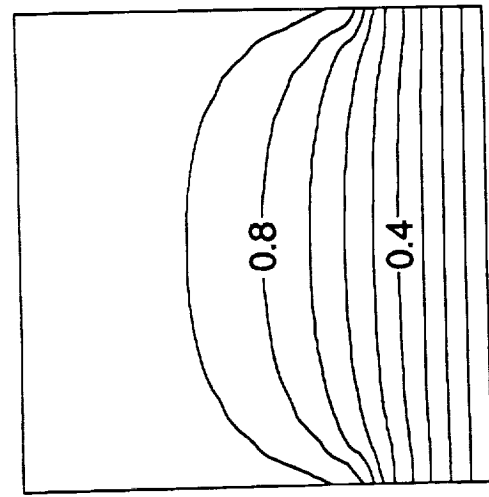


$Ra = 24000$

FIG. 4



VELOCITY



TEMPERATURE

FIG. 5

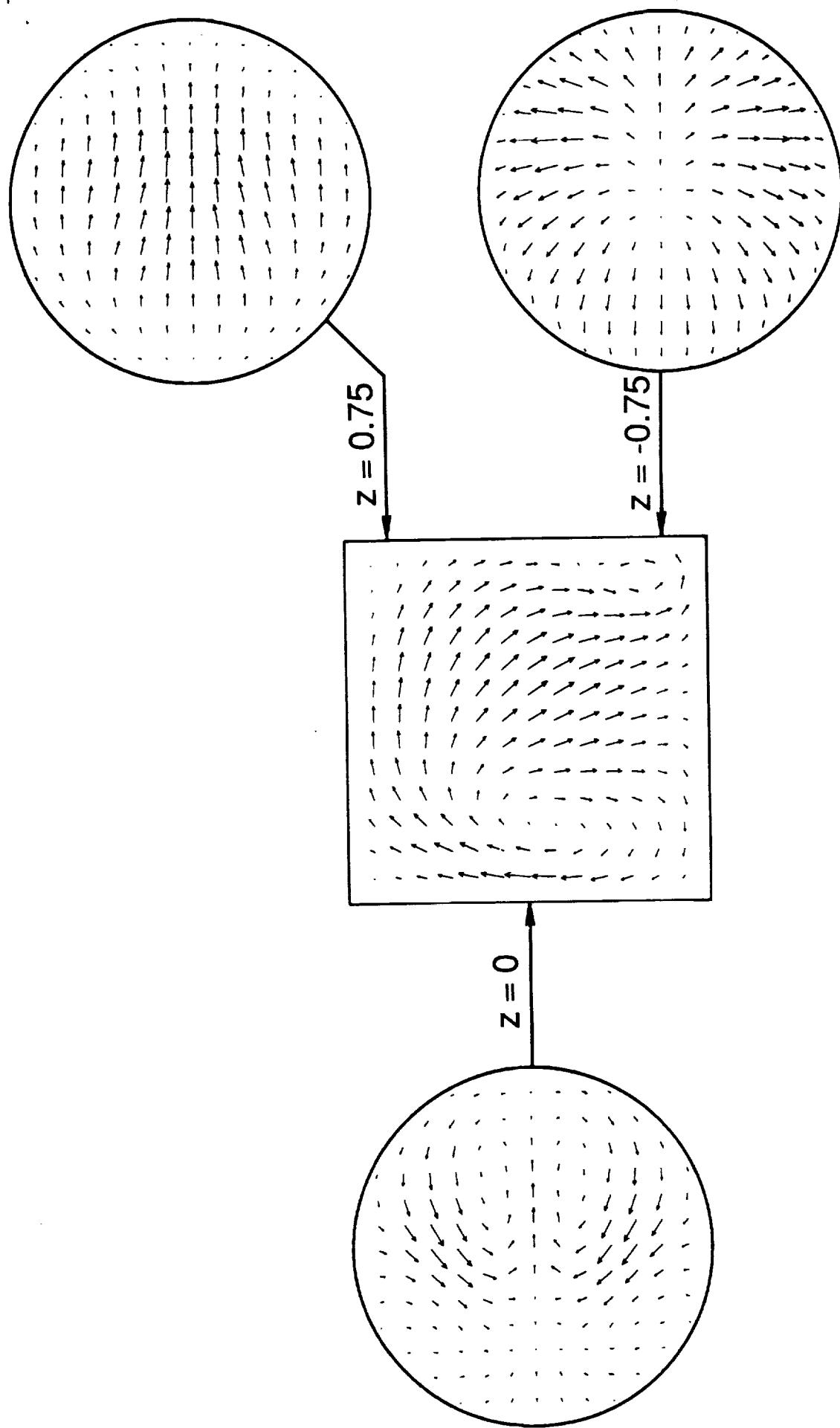
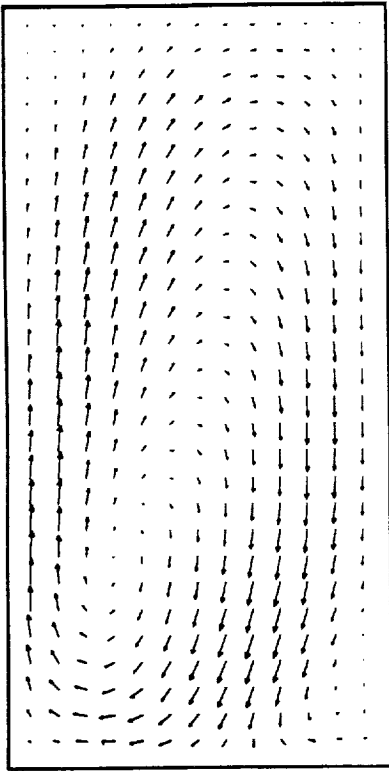
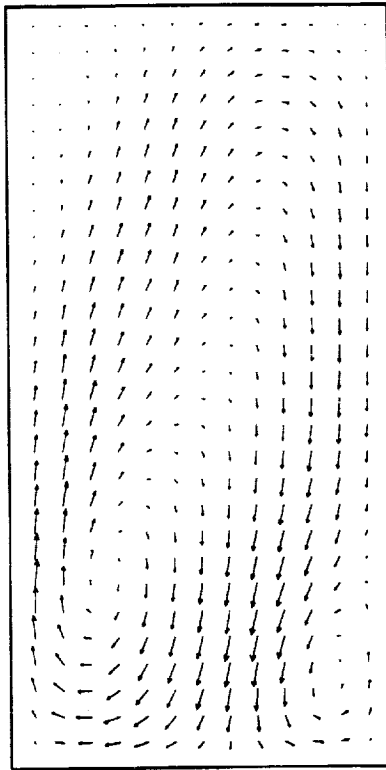


FIG. 6

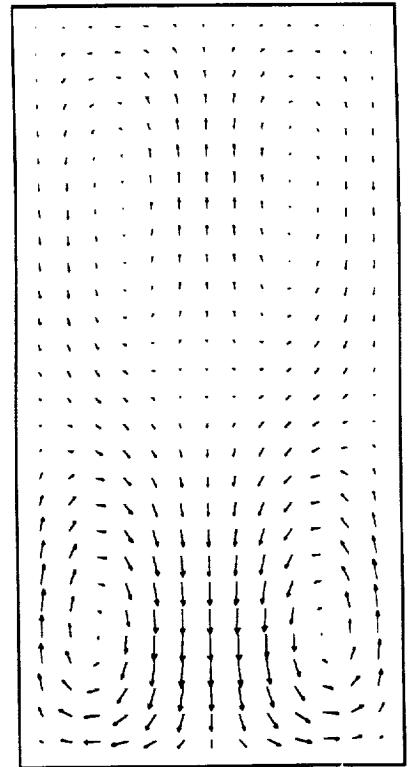
$\theta = 0^\circ$



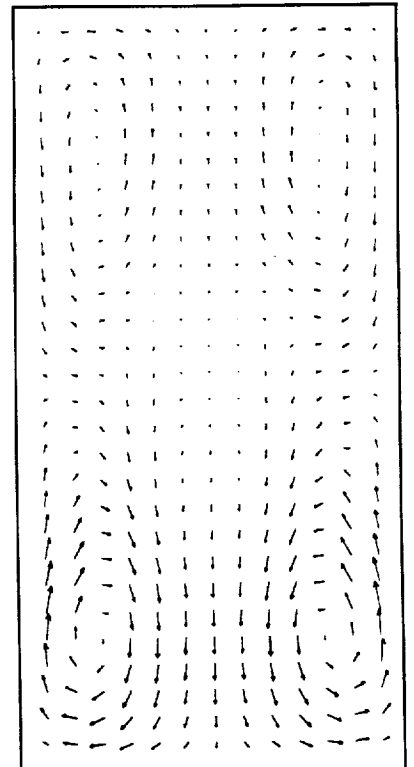
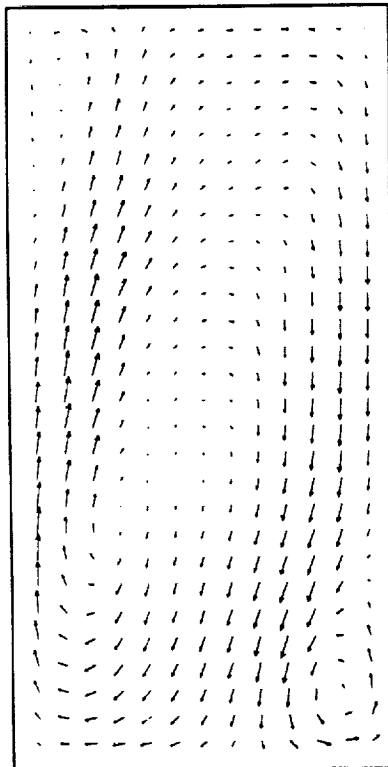
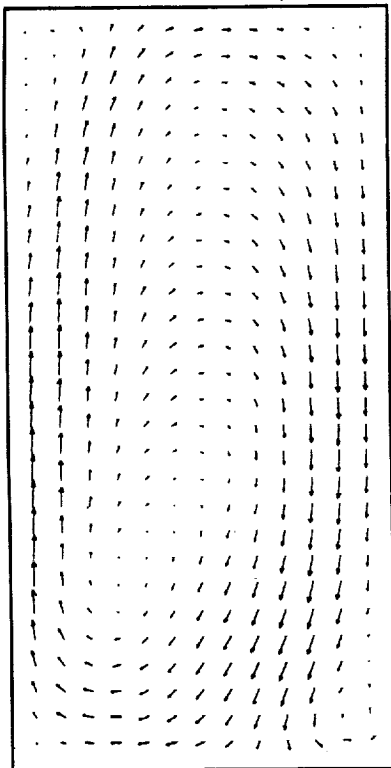
$\theta = 54^\circ$



$\theta = 90^\circ$



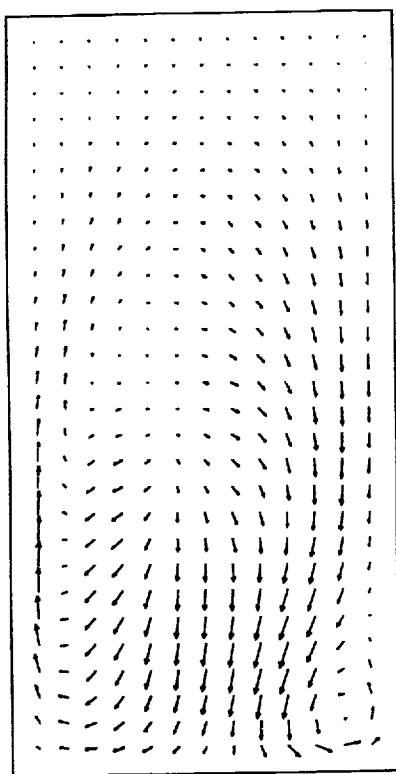
$Ra = 2500$



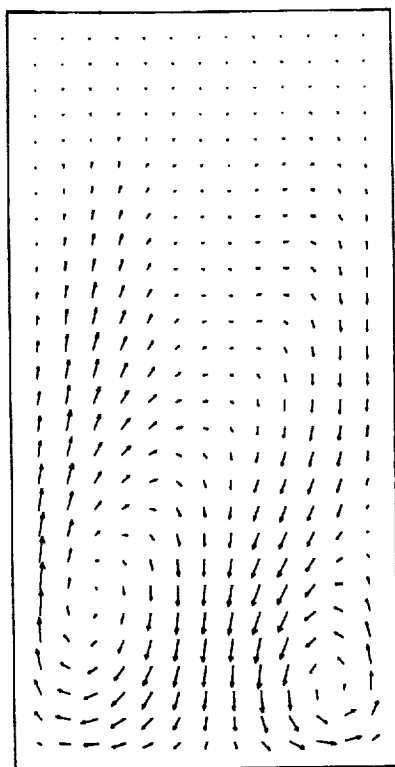
$Ra = 15000$

FIG. 7

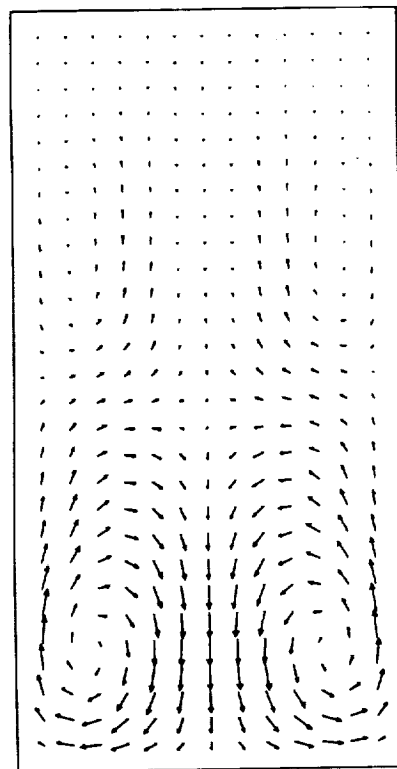
$\theta = 0^\circ$



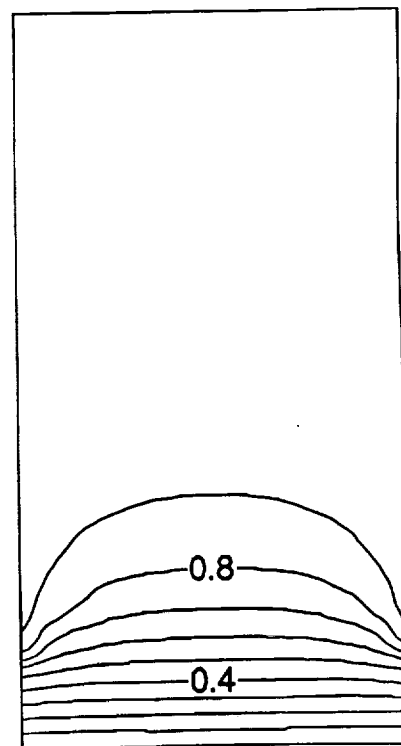
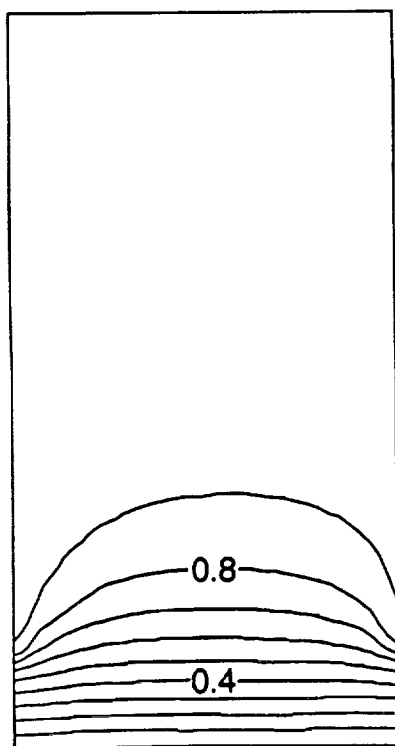
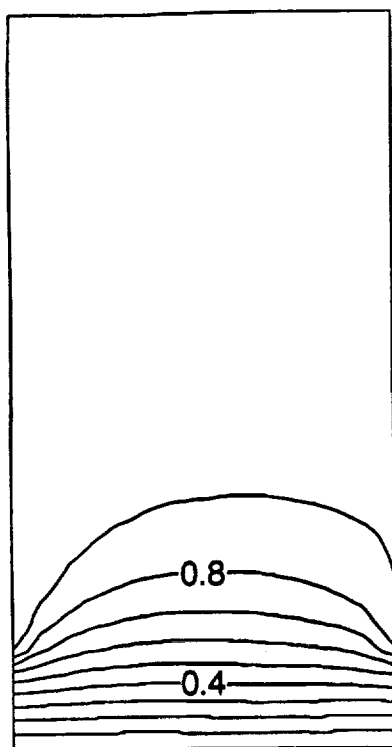
$\theta = 54^\circ$



$\theta = 90^\circ$



VELOCITY



TEMPERATURE

FIG. 8



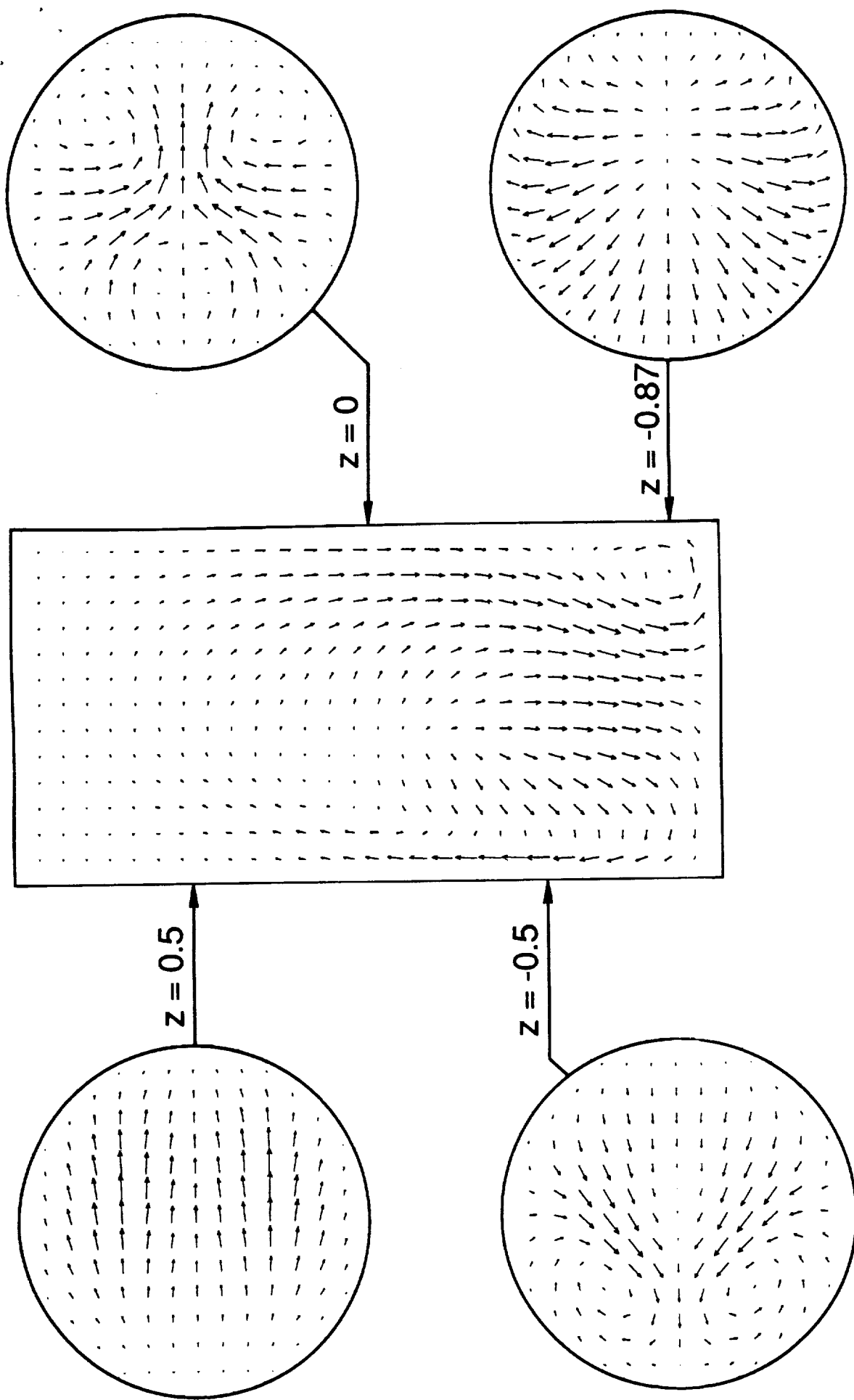
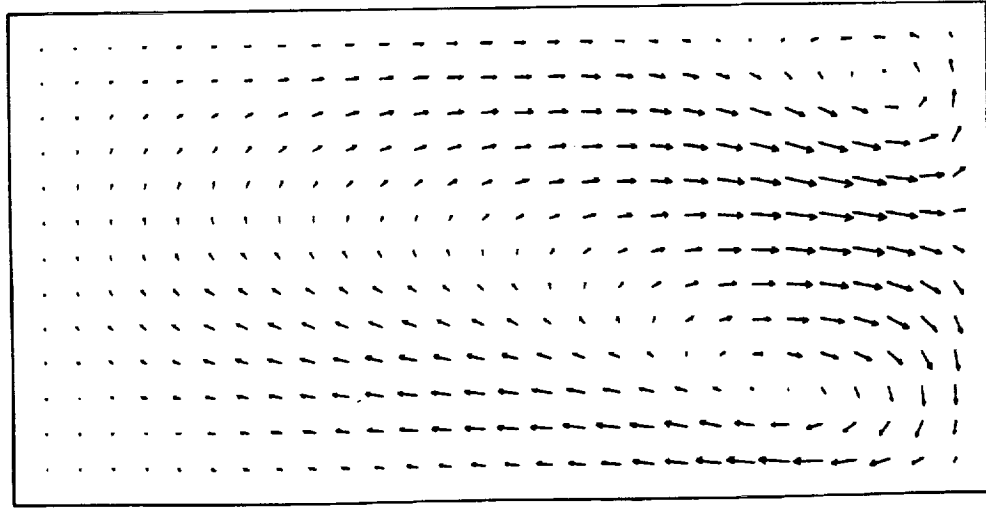
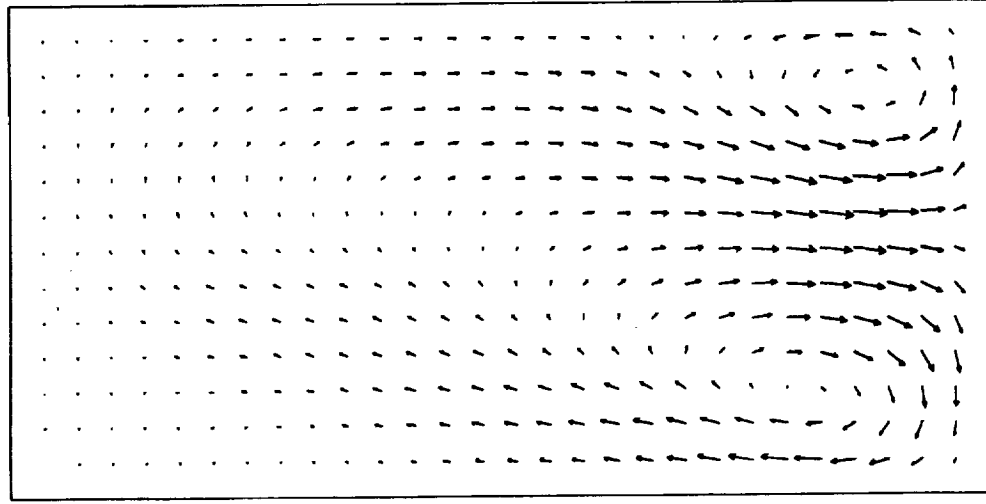


FIG. 9

$\theta = 0^\circ$



$\theta = 54^\circ$



$\theta = 90^\circ$

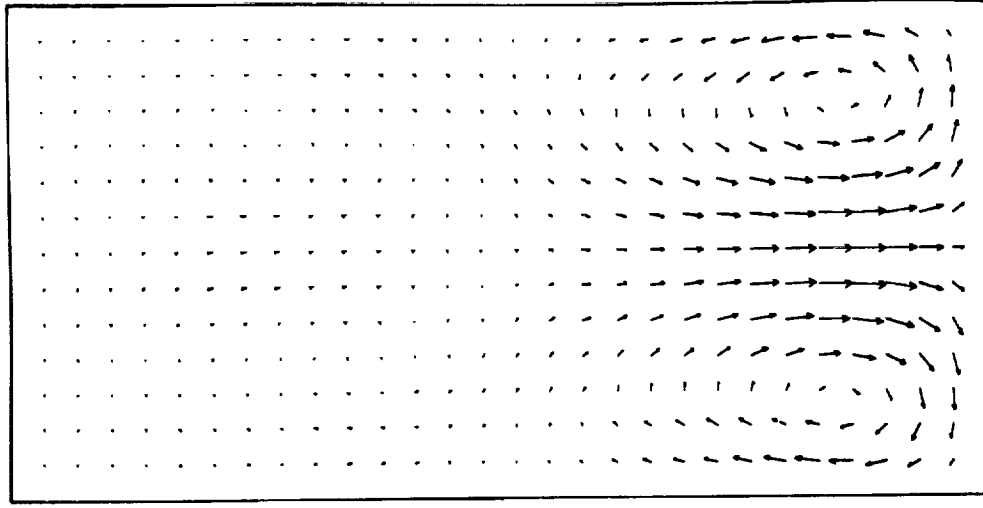


FIG. 10

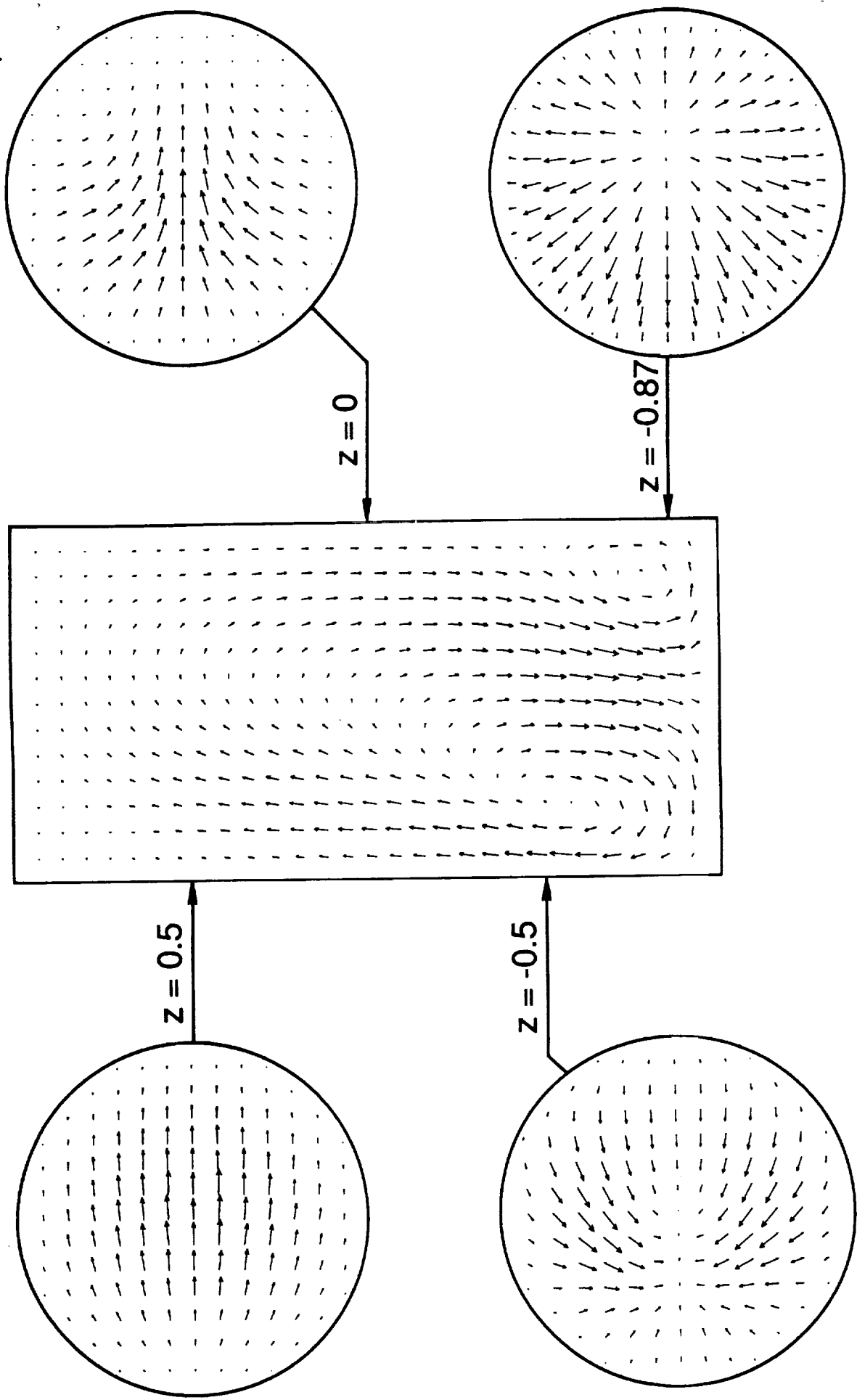
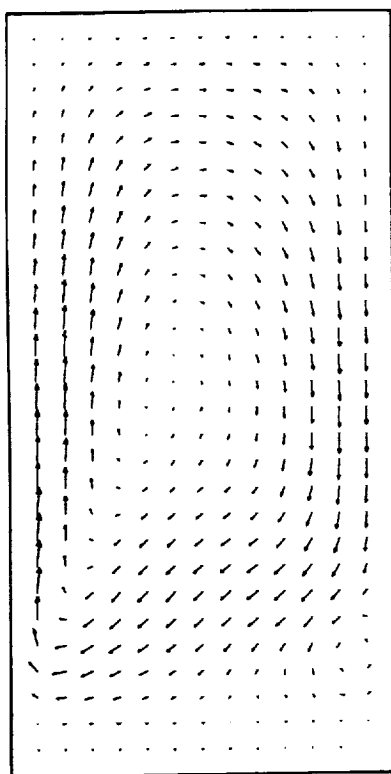
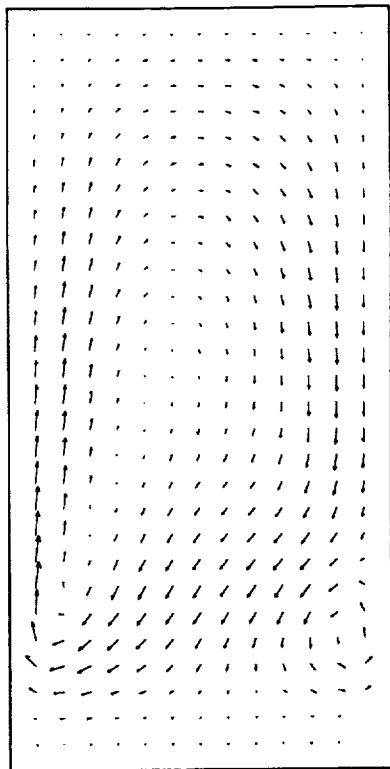


FIG. 11

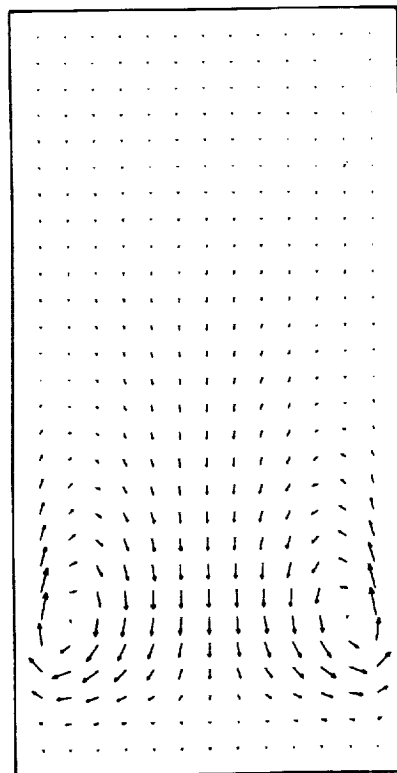
$\theta = 0^\circ$



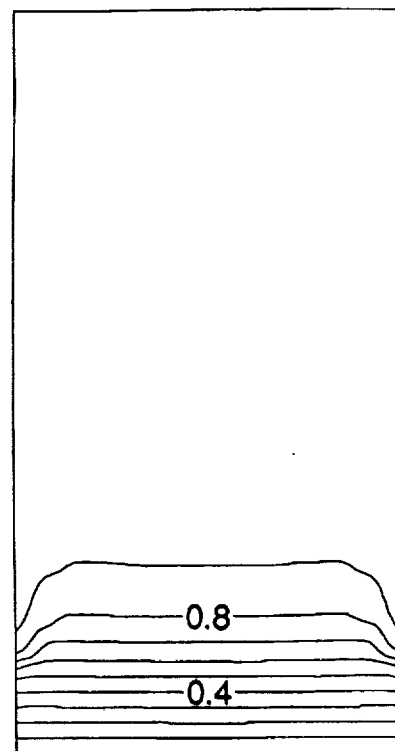
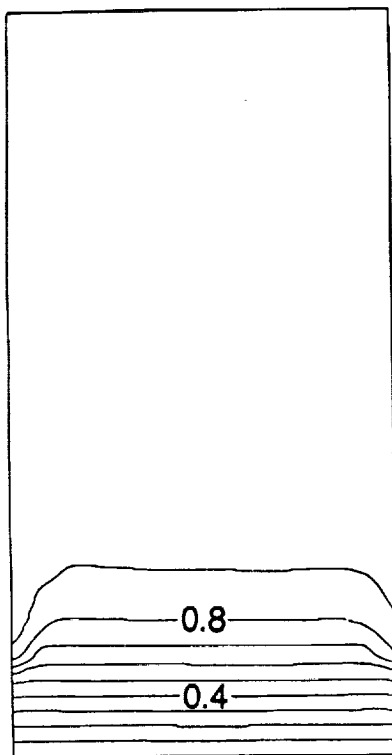
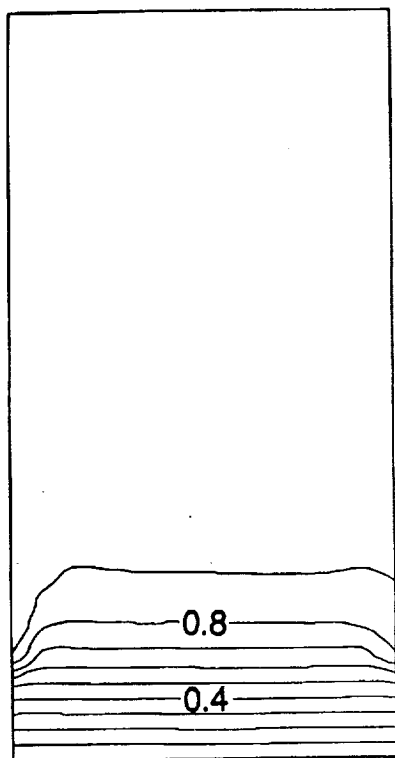
$\theta = 54^\circ$



$\theta = 90^\circ$



VELOCITY



TEMPERATURE

FIG. 12

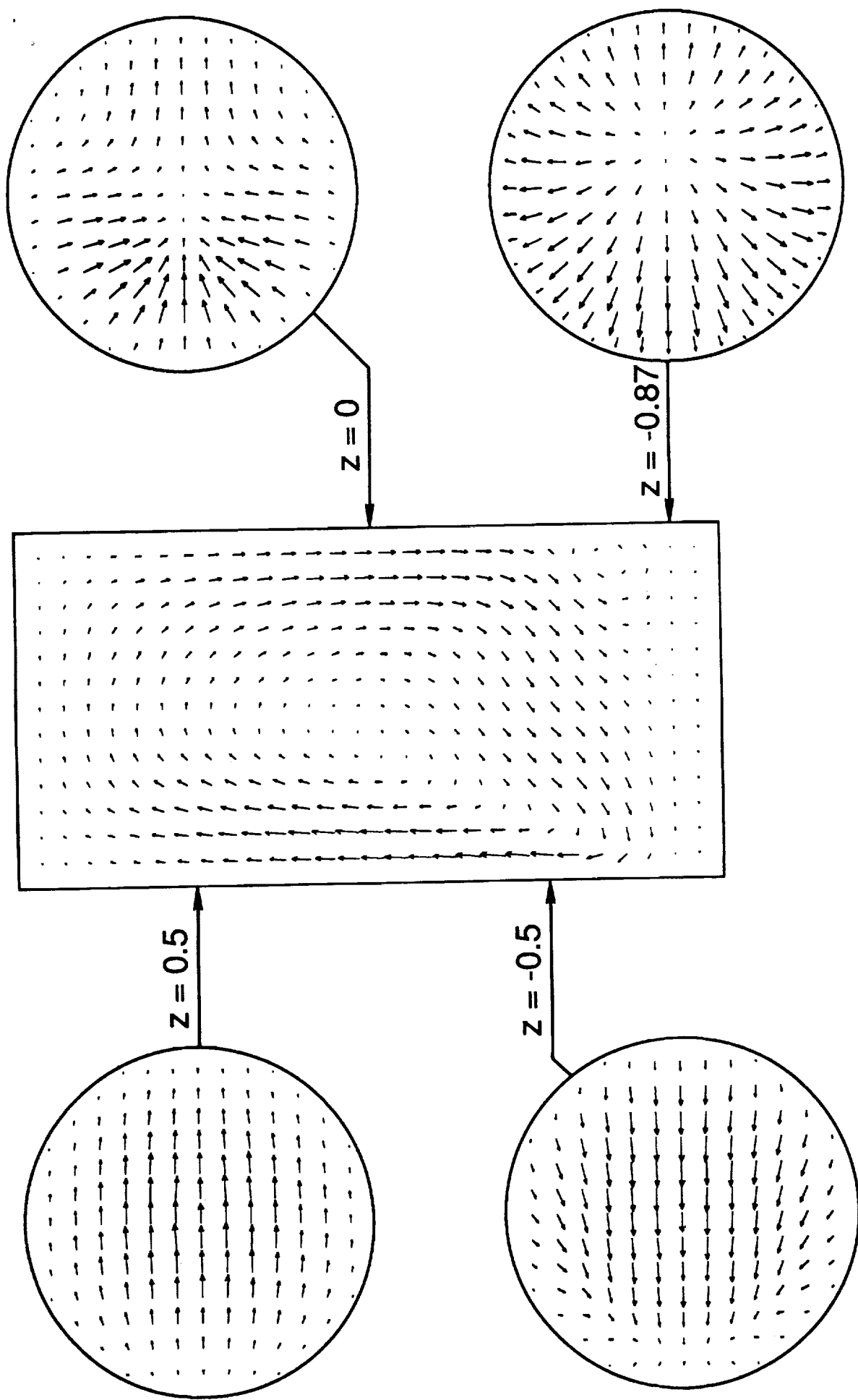


FIG. 13

**9. APPENDIX 1:**

**A Fourier-Chebyshev Pseudo-Spectral method for Solving Steady 3D Navier-Stokes and Heat Equations in Cylindrical Cavities, by J. P. Pulicani and J. Ouazzani (submitted to Computers and Fluids, August 1990).**

# **A Fourier-Chebyshev Pseudospectral Method for Solving Steady 3-D Navier-Stokes and Heat Equations in Cylindrical Cavities**

By

**J.P. Pulicani and J. Ouazzani**

Center for Microgravity and Materials Research, University of Alabama in Huntsville,  
Huntsville, Alabama 35899, USA

## **Abstract**

A Fourier-Chebyshev pseudospectral method for solving the steady 3-D Navier-Stokes and energy equations in cylindrical cavities is presented and discussed. The general method is pseudo-unsteady and uses a semi-implicit finite difference scheme for the time integration. The generalized ADI procedure is then applied to reduce the problem to successive solutions of one-dimensional problems. The spatial discretization uses a Fourier-Galerkin approximation in the periodic direction and a Chebyshev-collocation approximation in the other directions. Difficulties related to the pressure are surmounted by using the artificial compressibility method. A suitable variable change has been chosen to avoid the problem of singularity at the axis generated by cylindrical coordinates. The method is first tested on an advection-diffusion equation and then on the Navier-Stokes and heat equations. Finally, the method is illustrated by the problem of convection in a differentially heated fluid.

## 1. Introduction

For a long time numerical fluid mechanics has been focused mostly on two-dimensional models. Limitations related to the computer performance (i.e. excessive CPU time and large memory storage) have been among the main reasons for this trend, which has often prevented the solution of three-dimensional problems. However, two-dimensionality is difficult to achieve in real experiments. Nevertheless, increased research on numerical analysis and the improvement of computer performance permit more efficient solution of the complete 3-D Navier-Stokes and energy equations for several cases. Of the many numerical methods in use, those based on spectral approximations have met with increasing success over the last ten years. The principal attributes of spectral methods (see [1-4]) are their high accuracy and dual representation of the dependent variables in both physical and spectral space. Another advantage of these methods is their ability to accurately represent the solution with fewer collocation points than others (i.e. finite difference, finite elements, etc). This last advantage makes 3-D problems more tractable when using spectral methods. However, even though these methods have been extended to a large variety of 2-D physical problems (such as turbulence, channel flows, natural convection, crystal growth processes, etc) they have rarely been used for 3-D problems involving a cylindrical geometry. Most models assume axisymmetric conditions which result in 2-D problems.

In this paper we present and discuss a Fourier-Chebyshev pseudospectral method to solve the incompressible 3-D Navier-Stokes and energy equations. These equations are solved in a cylindrical geometry without the assumption of axisymmetry. The general method is pseudo-unsteady and uses a semi-implicit finite difference scheme for the time integration. The generalized ADI (Alternating Direction Implicit) procedure [2] is then applied to reduce the problem to the successive solution of one-dimensional problems. The spatial discretization uses a Fourier-Galerkin approximation in the periodic direction and a Chebyshev-collocation approximation in the other directions. Similar techniques were introduced for the solution of 2-D



steady binary gas mixture flows [5], and for the solution of a diffusion equation in a domain between two concentric spheres [3]. Difficulties related to the incompressibility condition and the pressure are surmounted by using the artificial compressibility method as used in [2,5]. Another method to maintain the incompressibility constraint is the use of the influence matrix technique [6]. This latter technique was applied for incompressible flows in cartesian and cylindrical geometries by [7] and in a rotating annulus by [8]. When using cylindrical coordinates without axisymmetry, the complexity is further increased by the presence of a singularity at the axis [7]. To eliminate this singularity, various methods such as the use of Cartesian coordinates [9,10], variable change [11], iterative technique [12] and special mesh [13], have been applied. In this paper we propose and assess two kinds of treatment. The first one is based on a variable change and the other on a device to avoid the points at the axis.

The method is first described and tested on an advection-diffusion equation and then on the Navier-Stokes and heat equations. Finally, the method is illustrated by a convection problem of a fluid in a horizontal differentially heated cylinder.

## 2. Numerical method for an advection-diffusion type equation

### 2.1 General method

For the description of the method, we consider the following problem :

$$\frac{\partial T}{\partial t} = \Delta T - \mathbf{V} \cdot \nabla T + F_T \quad , \quad t > 0 , \quad (2.1a)$$

where,

$$\Delta T = \frac{\partial^2 T}{\partial r^2} + \frac{1}{r} \frac{\partial T}{\partial r} + \frac{1}{r^2} \frac{\partial^2 T}{\partial \theta^2} + \frac{\partial^2 T}{\partial z^2}, \quad (2.1b)$$

$$V \cdot \nabla T = v_r \frac{\partial T}{\partial r} + \frac{v_\theta}{r} \frac{\partial T}{\partial \theta} + v_z \frac{\partial T}{\partial z}, \quad V = (v_r, v_\theta, v_z), \quad (2.1c)$$

for  $(r, \theta, z) \in \Omega = ]0, R[ \times [0, 2\pi[ \times ]-1, 1[$  (see Fig. 1) and the boundary and initial conditions :

$$a_\Gamma T|_\Gamma + b_\Gamma \frac{\partial T}{\partial n} \Big|_\Gamma = c_\Gamma, \quad \text{on } \Gamma = \partial\Omega, \quad (2.2a)$$

$$T = T_0, \quad \text{at } t = 0, \quad (2.2b)$$

where  $a_\Gamma, b_\Gamma, c_\Gamma, T_0, v_r, v_\theta, v_z$  and  $F_T$  are given functions and  $\partial/\partial n$  is the normal derivative. In real physical problems,  $V$  is the velocity.

Equation (2.1a) is discretized with respect to the time,  $t = n \delta t$ , using a semi-implicit scheme for the diffusive terms and explicit for the convective term :

$$(1 - \sigma \delta t \Delta) (T^{n+1} - T^n) = \delta t F^n, \quad (\sigma > 0), \quad (2.3a)$$

$$F^n = (\Delta T - V \cdot \nabla T + F_T)^n. \quad (2.3b)$$

Note that  $\sigma = 1/2$  corresponds to the Crank-Nicolson scheme.

The discrete equation (2.3) is solved by means of the generalized ADI procedure (as used in [2,5]) which reduces it to a set of one-dimensional problems. At each time step the following problem will be solved :

$$(1 - \sigma \delta t \Lambda_\theta) \Psi^* = \delta t F^n, \quad (2.4a)$$

$$(1 - \sigma \delta t \Lambda_z) \Psi^{**} = \Psi^*, \quad (2.4b)$$

$$(1 - \sigma \delta t \Lambda_r) \Psi^{***} = \Psi^{**}, \quad (2.4c)$$

$$T^{n+1} = T^n + \Psi^{***}, \quad (2.4d)$$

$$\Lambda_\theta = \frac{1}{r^2} \frac{\partial}{\partial \theta^2}, \quad \Lambda_z = \frac{\partial}{\partial z^2}, \quad \Lambda_r = \frac{\partial}{\partial r^2} + \frac{1}{r} \frac{\partial}{\partial r}. \quad (2.4e)$$

A standard Fourier-Galerkin approximation is employed for the solution of (2.4a). Thus,  $\Psi^*$  is expanded in a truncated Fourier series as follows

$$\Psi^*(r, \theta, z) = \sum_{k=-K/2}^{K/2-1} \widehat{\Psi}_k^*(r, z) e^{ik\theta}, \quad F^n(r, \theta, z) = \sum_{k=-K/2}^{K/2-1} \widehat{F}_k^n(r, z) e^{ik\theta}. \quad (2.5)$$

Equation (2.4a) can then be written as

$$\widehat{\Psi}_k^*(r, z) + \sigma \delta t \frac{k^2}{r^2} \widehat{\Psi}_k^*(r, z) = \delta t \widehat{F}_k^n(r, z), \quad (\text{for each harmonic } k), \quad (2.6)$$

with the Fourier coefficients  $\widehat{\Psi}_k^*$  as unknowns. From the solution of (2.6), it is then straightforward to deduce  $\Psi^*$  with (2.5). The values of  $\Psi^*$  have been calculated at the collocation points i.e.

$$\theta_k = 2\pi k / K, \quad k = 0, \dots, K-1. \quad (2.7)$$

The equations (2.4b) and (2.4c) are solved by means of a Chebyshev-collocation method.

For  $\Psi^{**}$ , we apply a Chebyshev polynomial expansion in the  $z$ -direction :

$$\Psi^{**}(r, \theta, z) = \sum_{m=0}^M \overline{\Psi_m^{**}}(r, \theta) T_m(z). \quad (2.8)$$

where  $\overline{\Psi_m^{**}}$  refers to the  $m^{\text{th}}$  Chebyshev coefficient and  $T_m$  to the  $m^{\text{th}}$  Chebyshev polynomial. The orthogonal collocation consists in expressing the derivatives at one collocation point in terms of values of the function at all points. For instance the second derivative is expressed by

$$\frac{\partial^2 \Psi^{**}}{\partial z^2}(r, \theta, z_j) = \sum_{\mu=0}^M d(z_j, z_\mu)^{(2)} \Psi^{**}(r, \theta, z_\mu), \quad (2.9)$$

$$\text{at the collocation points : } z_j = \cos(\pi j / M), \quad j = 0, \dots, M. \quad (2.10)$$

The coefficients  $d(z_j, z_\mu)^{(2)}$  are obtained by using the orthogonality property of the Chebyshev polynomials and the usual trigonometric formulas [3,5]. In matrix-vector notation, the equation (2.9) can be written as

$$\frac{\partial^2 \phi^{**}}{\partial z^2}(r, \theta, z_j) = \mathcal{D} \phi^{**}, \quad \mathcal{D} = [d(z_j, z_\mu)^{(2)}], \quad (2.11a)$$

$$\phi^{**} = [\Psi^{**}(r, \theta, z_0), \dots, \Psi^{**}(r, \theta, z_\mu), \dots, \Psi^{**}(r, \theta, z_M)]^T. \quad (2.11b)$$

Then by using (2.11) in the left-hand side of (2.4b), we obtain the algebraic system

$$\mathcal{M} \phi^{**} = \phi^*, \quad \mathcal{M} = I - \sigma \delta t \mathcal{D}, \quad (2.12a)$$

$$\phi^* = [\Psi^*(r, \theta, z_0), \dots, \Psi^*(r, \theta, z_\mu), \dots, \Psi^*(r, \theta, z_M)]^T. \quad (2.12b)$$

For the solution of (2.4c), the technique is identical, but a Chebyshev polynomial expansion is applied in the  $r$ -direction for  $\Psi^{***}$ , that is

$$\Psi^{***}(\xi, \theta, z) = \sum_{n=0}^N \overline{\Psi_n^{***}}(\theta, z) T_n(\xi), \quad (2.13)$$

where  $\xi$  refers to the transformed plane  $\xi = 2r/R - 1$  ( $-1 \leq \xi \leq 1$  and  $0 \leq r \leq R$ ).

The first and second derivatives of  $\Psi^{***}$  are then written as

$$\frac{\partial^p \Psi^{***}}{\partial \xi^p}(\xi_i, \theta, z) = \sum_{\eta=0}^N a(\xi_i, \xi_\eta)^{(p)} \Psi^{***}(\xi_\eta, \theta, z), \quad p = 1, 2, \quad (2.14)$$

$$\xi_i = \cos(\pi i / N), \quad r_i = R(\xi_i - 1) / 2, \quad i = 0, \dots, N, \quad (2.15)$$

$$\left( \frac{\partial^2 \Psi^{***}}{\partial r^2} + \frac{1}{r_i} \frac{\partial \Psi^{***}}{\partial r} \right)(r_i, \theta, z) = \left( \lambda^2 \frac{\partial^2 \Psi^{***}}{\partial \xi^2} + \frac{\lambda}{r_i} \frac{\partial \Psi^{***}}{\partial \xi} \right)(\xi_i, \theta, z) = \mathcal{A} \phi^{***}, \quad (2.16a)$$

$$\mathcal{A} = \lambda^2 \left[ a(\xi_i, \xi_\eta)^{(2)} \right] + \frac{\lambda}{r_i} \left[ a(\xi_i, \xi_\eta)^{(1)} \right], \quad \lambda = \left( \frac{2}{R} \right), \quad (2.16b)$$

$$\phi^{***} = [ \Psi^{***}(\xi_0, \theta, z), \dots, \Psi^{***}(\xi_\eta, \theta, z), \dots, \Psi^{***}(\xi_N, \theta, z) ]^T. \quad (2.16c)$$

We obtain an algebraic system by using (2.16) in the left-hand side of (2.4c) in the form :

$$\mathcal{N} \phi^{***} = \phi^{**}, \quad \mathcal{N} = I - \sigma \delta t \mathcal{A}, \quad (2.17a)$$

$$\phi^{**} = [ \Psi^{**}(\xi_0, \theta, z), \dots, \Psi^{**}(\xi_\eta, \theta, z), \dots, \Psi^{**}(\xi_N, \theta, z) ]^T. \quad (2.17b)$$

The first and last equations in (2.12) and (2.17) are replaced by the boundary conditions. If the boundary conditions are not time-dependent and if the initial condition satisfies these boundary

conditions, then the boundary conditions for  $\phi^{**}$  and  $\phi^{***}$  are homogeneous. Still that in all cases, the inversion of the resulting matrix  $\mathcal{M}$  and  $\mathcal{N}$  is made only once before the time integration begins. Thus, only matrix vector products have to be performed at each time-step, that is :  $\phi^{**} = \mathcal{M}^{-1} \phi^*$ , then  $\phi^{***} = \mathcal{N}^{-1} \phi^{**}$  and finally  $T^{n+1}$  with (2.4d).

The right hand side of (2.4a) is evaluated by the standard pseudospectral technique [1]. The derivatives are performed in the spectral space and the products in the physical one. These two spaces are connected through a FFT algorithm [14]. Note that the FFT algorithm is more efficient than the direct matrix-vector multiplication method only when the number of collocation points is greater than 30.

When using cylindrical coordinates there is a difficulty associated with the presence of the singularity at the axis (for  $1/r \rightarrow \infty$  when  $r \rightarrow 0$ ). This difficulty arises because the axis is a boundary of the computational domain only by construction of the coordinate system. Obviously, this problem can be alleviated when the value of  $T(r=0, \theta, z)$  or its derivative is known at the axis (for instance if the solution is supposed to be axisymmetric or if a natural boundary condition exists to be imposed at this axis). For most physical problems, the axis cannot be considered as a boundary in the problem (2.1); therefore a special treatment to eliminate this singularity is required. In this paper we propose two kinds of treatment. One is based on a variable change and the other on a distribution of points excluding the axis.

## 2.2 Treatment of the singularity by using a variable change

The problem of singularity can be avoided by applying to equation (2.1) the following change of variable :

$$T(r, \theta, z) = r^\beta \tilde{T}(r, \theta, z) \quad , \quad \beta < 0. \quad (2.18)$$

The idea for such a variable change came from a private conversation with Dr R Peyret (University of Nice, France). A similar variable change for a functional equation has also been used in [15, p.1104]. The main advantage of the variable change (2.18) is that  $\tilde{T}(r, \theta, z) = 0$  at  $r = 0$  for  $\beta < 0$ . For the problem (2.1)-(2.2) it is normally not necessary to use the same variable change for the velocities since they are given functions. But in order to apply the method to the Navier-Stokes and energy equations, we enforce the following identities :

$$v_r(r, \theta, z) = r^\beta \tilde{v}_r(r, \theta, z), \quad v_\theta(r, \theta, z) = r^\beta \tilde{v}_\theta(r, \theta, z) \text{ and } v_z(r, \theta, z) = r^\beta \tilde{v}_z(r, \theta, z). \quad (2.19)$$

Applying these variable changes to (2.1a) it yields

$$\frac{\partial \tilde{T}}{\partial t} = \tilde{F} = r^{-\beta} (\Delta T - \mathbf{V} \cdot \nabla T + F_T), \quad (2.20a)$$

$$r^{-\beta} \Delta T = \frac{\partial^2 \tilde{T}}{\partial r^2} + \frac{(2\beta+1)}{r} \frac{\partial \tilde{T}}{\partial r} + \frac{\beta^2}{r^2} \tilde{T} + \frac{1}{r^2} \frac{\partial^2 \tilde{T}}{\partial \theta^2} + \frac{\partial^2 \tilde{T}}{\partial z^2}, \quad (2.20b)$$

$$r^{-\beta} \mathbf{V} \cdot \nabla T = r^\beta \tilde{v}_r \frac{\partial \tilde{T}}{\partial r} + \beta r^{\beta-1} \tilde{v}_r \tilde{T} + r^{\beta-1} \tilde{v}_\theta \frac{\partial \tilde{T}}{\partial \theta} + r^\beta \tilde{v}_z \frac{\partial \tilde{T}}{\partial z}. \quad (2.20c)$$

Thus, equation (2.20) remains to be solved for  $\tilde{T}$ . Furthermore, due to the change of variable (2.18), the boundary and initial conditions are now :

$$a_{\Gamma_1} \tilde{T}|_{\Gamma_1} + b_{\Gamma_1} \left( r^{-\beta} \frac{\partial(r^\beta)}{\partial n} \tilde{T} + \frac{\partial \tilde{T}}{\partial n} \right) \Big|_{\Gamma_1} = r^{-\beta} c_{\Gamma_1}, \quad \text{on } \Gamma_1 \quad (2.21a)$$

$$\tilde{T}|_{\Gamma_2} = 0, \quad \text{on } \Gamma_2, \quad (2.21b)$$

$$\tilde{T} = r^{-\beta} T_0, \quad \text{at } t = 0, \quad (2.21c)$$

where  $\Gamma_2$  refers to the boundary  $r = 0$  (without the points at  $z = \pm 1$ ) and  $\Gamma_1 = \Gamma - \Gamma_2$ .

It is now easy to apply the method described in the previous section. At each time step the problem (2.4) is solved by replacing  $F^n$  by  $\tilde{F}^n$  (corresponding to  $\tilde{F}$  at  $t = n \delta t$ ),  $T$  by  $\tilde{T}$ , and by taking

$$\Lambda_r = \frac{\partial^2}{\partial r^2} + \frac{(2\beta+1)}{r} \frac{\partial}{\partial r} + \frac{\beta^2}{r^2} \text{ in (2.4e).}$$

It is easy to obtain  $T$  from (2.18), after having calculated  $\tilde{T}$  (except at  $r = 0$ ). Note that the value of  $T$  at the axis can then be found by interpolation.

### 2.3 Treatment of the singularity by omitting the axis

In this section we propose another method to deal with the singularity which involves excluding the points at the axis. That can be done using the Gauss-Radau collocation points in the  $r$ -direction, *between 0 and R*, as suggested in [4, p.91], or by using an even number of Gauss-Lobatto collocation points in the  $r$ -direction, *between  $-R$  and  $R$* , as proposed in [16] for a simple problem. Here we apply the latter technique to the general method described in section 2.1 by creating a new computational interval  $[-R, R]$ , which corresponds to the diameter of the cylinder. Note that we are not forming the interval  $[-R, R]$  by extending each radial interval from  $[0, R]$  but by joining one radial interval  $[0, R]$  at the angle  $\theta$  with another at  $(\theta + \pi)$  for  $\theta \in [0, \pi]$ . Thus, the radial dependence of the functions is approximated by a Chebyshev expansion between  $-R$  and  $R$  on a well defined distribution of points which are physically meaningful. The singularity still remains when the axis belongs to the computational domain. However, by choosing an even number of Gauss-Lobatto-Chebyshev collocation points, the axis is automatically excluded. The problem of enforcing a boundary condition for the  $r$ -direction at the axis, when using Gauss-Lobatto points, is thus avoided. Furthermore, this device allows us to calculate the derivative with



respect to the  $r$ -direction in the right-hand-side  $F^n$  of (2.3a) and the term  $\Psi^{***}$  in (2.4c) without taking into account the axis. For instance, for the evaluation of  $\Psi^{***}$  we need to discretize the equation (2.4c). This requires the use of the formula (2.16) in which the collocation points, between  $-R$  and  $R$ , write as :

$$r_i = R \xi_i , \quad \xi_i = \cos(\pi i / N) , \quad i = 0, \dots, N. \quad (2.22)$$

It follows that in (2.16a) :

$$\lambda = 1 / R \quad (2.23)$$

From a practical point of view, values of  $N$ , such that  $N=5^n 3^p$  ( $n$  and  $p$  being integers), must be chosen when using the FFT algorithm [14] ( to use the pseudospectral technique for the derivatives relative to the  $r$ -direction in  $F^n$ ) in order to avoid the points at the axis. Of course, to remove this constraint on  $N$ , it is always possible to use formulas of type (2.11). In this case, the FFTs would be replaced by products of matrices (only for the calculation of the derivatives related to the  $r$ -direction).

#### 2.4 Assessment of these methods with an analytical solution

In order to evaluate the above methods on problem (2.1)-(2.2), we have chosen the exact solution

$$T_{\text{ex}}(r, \theta, z) = F(r) H(\theta) G(z) + C , \quad (C \in \mathbb{R}) , \quad (2.24a)$$

$$F(r) = r^7 (r - R) ; \quad G(z) = (z^2 - 1) (z^8 + 1) ; \quad H(\theta) = \sin \theta + \cos(9\theta - 1) , \quad (2.24b)$$

from which we define the Dirichlet boundary conditions

$$T|_{\Gamma_1} = C, \quad \text{on } \Gamma_1. \quad (2.25)$$

The velocities are then

$$v_{r_{ex}} = \sin \theta \, r (R^2 - r), \quad (2.26a)$$

$$v_{\theta_{ex}} = \cos \theta \, (2 \, r \, R^2 - r^2 (3 + 2z)), \quad (2.26b)$$

$$v_{z_{ex}} = \sin \theta \, r (1 - z^2). \quad (2.26c)$$

It then follows that  $F_T$  is given by

$$F_T = V \cdot \nabla T - \Delta T. \quad (2.27)$$

The chosen initial condition is

$$T_0(r, \theta, z) = T_{ex}(r, \theta, z) + 80 (R - r)^5 r (z^3 - z) \sin^4 \theta. \quad (2.28)$$

The computations were carried out on a Cray XMP computer for the case  $C=1$  and  $R=1$ .

In the tables presented below, the residual of  $\vartheta$  (denoted  $R_\vartheta$ ), the  $L^2$  and Sup errors of  $\vartheta$  (denoted  $E_\vartheta^{L^2}$  and  $E_\vartheta^{sup}$  respectively) are displayed. Note that  $R_\vartheta$ ,  $E_\vartheta^{L^2}$  and  $E_\vartheta^{sup}$  are calculated on the collocation points of  $\vartheta$  and that  $\vartheta = \{T, v_r, v_\theta, v_z\}$ . Furthermore

$$R_\vartheta = \text{Max}_{i,k,j} \left[ \frac{|\vartheta(r_i, \theta_k, z_j)^{n+1} - \vartheta(r_i, \theta_k, z_j)^n|}{\delta t} \right], \quad (2.29)$$

$$E_{\vartheta}^{L2} = \sqrt{\frac{1}{(N-1)K(M-1)} \sum_{i=1}^{N-1} \sum_{k=1}^K \sum_{j=1}^{M-1} |\vartheta_{NKM}(r_i, \theta_k, z_j) - \vartheta_{ex}(r_i, \theta_k, z_j)|^2}, \quad (2.30)$$

$$E_{\vartheta}^{sup} = \text{Max}_{i,k,j} |\vartheta_{NKM}(r_i, \theta_k, z_j) - \vartheta_{ex}(r_i, \theta_k, z_j)|, \quad (2.31)$$

with  $i=1, \dots, N-1$ ,  $k=1, \dots, K$ ,  $j=1, \dots, M-1$ ;  $\vartheta_{ex}$  = exact solution of  $\vartheta$  and  $\vartheta_{NKM}$  = numerical solution of  $\vartheta$ .

The problem (2.1)-(2.2) was solved by means of the following methods :

- Method I described in section 2.1 by enforcing the real value of T at the axis (i.e.  $T=C$  at  $r=0$ ),
- Method II described in section 2.2,
- Method III described in section 2.3.

Note that method I is not applicable to real problems because the values of independent variables are not known at the axis. This method is nevertheless presented in this paper in order to assess the effect of the variable change used in the method II to treat the singularity (effect on the accuracy and rate of convergence).

In all tables, we denote :

- $N_r$  the number of collocation points between  $r = 0$  and  $R$ , for methods I and II,  
and between  $r = -R$  and  $R$ , for method III.
- $K_{\theta}$  the number of collocation points between  $\theta = 0$  and  $2\pi$ , for methods I and II,  
and between  $\theta = 0$  and  $\theta = \pi$  for method III.
- $M_z$  the number of collocation points between  $z = -1$  and  $1$  for all methods.

Table 1 presents results concerning the convergence (towards the steady state) and the accuracy of all three methods, after 200 time cycles. These results correspond to a parameter  $\sigma$  (occurring in (2.3)) fixed to 0.5 and  $\beta$  equal to  $-1$  (occurring in (2.18) and (2.19)). For approximately the same number of points, the accuracy is better with methods I and II than method III. With methods I and II, the machine accuracy ( $\approx O(10^{-12})$ ) is reached with only  $10 \times 20 \times 13$  (i.e.  $N_r \times K_\theta \times M_z$ ) points, after 200 iterations. For method III, when taking  $N_r \times K_\theta \times M_z = 26 \times 10 \times 13$ , the error stagnates at  $O(10^{-8})$  after 200 time cycles. To decrease the error to  $O(10^{-10})$  with this method, the number of points must be increased to  $N_r \times K_\theta \times M_z = 46 \times 10 \times 13$ . Despite the increase of points in the  $r$ -direction to  $N_r = 46$ , the rate of convergence has not diminished significantly (residual  $R_T = 9.6 \cdot 10^{-10}$  after 200 iterations). Whereas, in methods I and II, the increase of polynomials in the  $r$ -direction affects much more the speed of convergence. Table 1 shows that for these methods, the residual after 200 time cycles, is  $O(10^{-4})$  when  $N_r = 21$ . To reach an accuracy of  $O(10^{-12})$  with such number of points in the  $r$ -direction, 500 iterations are needed. When increasing the number of polynomials in the  $r$ -direction, the density of points near the origin, for methods I and II, is significantly increased as compared to the one in method III. This leads to much stronger values of the term " $1/r$ " near the axis in the two first methods than in the last one. Therefore, for stability reasons, the time step for methods I and II is smaller than the one for method III. This restriction on the time step  $\delta t$  decreases the speed of convergence of method I and II relative to method III. A rigorous stability study here is quite complex and would be beyond the scope of this paper. However, we must point out that the method III gives good results for solutions (2.24)-type for they do not involve strong gradients near the axis (in (2.24),  $\partial T / \partial r = 0$  at the axis). When the solutions are stiffer close to the axis, method III is not as well adapted as method II, because the number of polynomials needed to represent the solution accurately becomes unacceptable. One possibility to overcome this difficulty, would be to use a mapping procedure as in [3,17], to concentrate the distribution of points in zones where sharp gradients in the solution are exhibited. For approximatively the same number of

polynomials, the CPU time per time step needed for technique III is about 1.5 times higher than the one required by the other methods. This difference is mostly due to the switches between the two kinds of coordinate system associated with this method (see section 2.3). These switches also generate programming difficulties and memory problems. Table 1 shows that methods I and II have the same order of accuracy but that the rate of convergence is greater with II than I. This difference of speed is probably due to the better properties of the ADI operator  $(1 - \sigma \delta t \Lambda_r)$  following the variable change used in section 2.2. This difference has been found to be smaller when the number of points is higher.

Finally, for more flexibility and efficiency, we have chosen the technique II to extend the method to Navier-Stokes and energy equations. By exploring different values of  $\beta$ , we have noted that for  $\beta > -1$  the accuracy is poor and for  $\beta < -1$  the method is unstable (even when using very small time steps). In fact, the only value for which the method II works efficiently is  $\beta = -1$ . Table 2 shows the results of method II for different numbers of points and values of  $\sigma$ . The value  $\sigma = 0.5$  was found to optimize the rate of convergence. In [3] for the solution of a diffusion equation in a domain between two concentric spheres the optimal value of  $\sigma$  was 0.6. In the remainder of this paper we shall use  $\beta = -1$  and  $\sigma = 0.5$ .

### 3. Numerical method for the Navier-Stokes and heat equations

#### 3.1 Description of the method

In this section a method for solving Boussinesq-Navier-Stokes and energy type equations is presented. We use primitive variables [18] in a fixed reference frame. The problem to be solved will be the transport-diffusion type equation (2.1) coupled with

$$\frac{\partial v_z}{\partial t} = \text{Pr} \Delta v_z - \mathbf{V} \cdot \nabla v_z - \frac{\partial p}{\partial z} + \cos(a\varphi + b) \text{Pr} \text{Ra} T + F_{v_z} , \quad (3.1a)$$

$$\frac{\partial v_r}{\partial t} = \text{Pr} \Delta v_r - \mathbf{V} \cdot \nabla v_r - \frac{\partial p}{\partial r} + \sin(c\phi + d) \sin(e\theta + f) \text{Pr Ra } T + F_{v_r} , \quad (3.1b)$$

$$\frac{\partial v_\theta}{\partial t} = \text{Pr} \Delta v_\theta - \mathbf{V} \cdot \nabla v_\theta - \frac{1}{r} \frac{\partial p}{\partial \theta} + \sin(c\phi + d) \cos(e\theta) \text{Pr Ra } T + F_{v_\theta} , \quad (3.1c)$$

$$\nabla \cdot \mathbf{V} = \frac{v_r}{r} + \frac{\partial v_r}{\partial r} + \frac{1}{r} \frac{\partial v_\theta}{\partial \theta} + \frac{\partial v_z}{\partial z} = 0 , \quad (3.1d)$$

where  $\Delta v_z$  and  $\mathbf{V} \cdot \nabla v_z$  are obtained by replacing  $T$  by  $v_z$  in (2.1b), (2.1c) and (2.1d), and

$$\Delta v_r = \frac{\partial^2 v_r}{\partial r^2} + \frac{1}{r} \frac{\partial v_r}{\partial r} - \frac{v_r}{r^2} + \frac{1}{r^2} \frac{\partial^2 v_r}{\partial \theta^2} + \frac{\partial^2 v_r}{\partial z^2} - \frac{2}{r^2} \frac{\partial v_\theta}{\partial \theta} , \quad (3.1e)$$

$$\Delta v_\theta = \frac{\partial^2 v_\theta}{\partial r^2} + \frac{1}{r} \frac{\partial v_\theta}{\partial r} - \frac{v_\theta}{r^2} + \frac{1}{r^2} \frac{\partial^2 v_\theta}{\partial \theta^2} + \frac{\partial^2 v_\theta}{\partial z^2} + \frac{2}{r^2} \frac{\partial v_r}{\partial \theta} , \quad (3.1f)$$

$$\mathbf{V} \cdot \nabla v_r = v_r \frac{\partial v_r}{\partial r} + \frac{v_\theta}{r} \frac{\partial v_r}{\partial \theta} - \frac{v_\theta^2}{r} + v_z \frac{\partial v_r}{\partial z} , \quad (3.1g)$$

$$\mathbf{V} \cdot \nabla v_\theta = v_r \frac{\partial v_\theta}{\partial r} + \frac{v_\theta}{r} \frac{\partial v_\theta}{\partial \theta} + \frac{v_r v_\theta}{r} + v_z \frac{\partial v_\theta}{\partial z} . \quad (3.1h)$$

The above problem is solved in the domain  $\Omega_1$ , with  $a, b, c, d, e, f, \phi, \text{Pr}$  and  $\text{Ra}$  as parameters, and  $F_{v_z}, F_{v_r}, F_{v_\theta}$  as given functions. The initial and boundary conditions will be defined later for each specific problem. The equations (2.1) and (3.1a,b,c) are solved by using the technique explained in section 2.2 with the variable changes (2.18) and (2.19) for  $T, v_r, v_\theta$  and  $v_z$ , and

$p(r, \theta, z) = r^\beta \tilde{p}(r, \theta, z)$ , when  $\beta = -1$ . For the problem (3.1), the typical numerical difficulties lie in the constraint  $\nabla \cdot \mathbf{V} = 0$  and the lack of boundary conditions for the pressure. In the steady case, these difficulties can be overcome by using the artificial compressibility method [2,5], which involves a perturbed continuity equation

$$\frac{\partial p}{\partial t} + \varepsilon \nabla \cdot \mathbf{V} = 0, \quad (3.2)$$

where  $\varepsilon$  is a strictly positive constant. This equation has no physical meaning before the steady state  $\partial / \partial t = 0$  is reached. Another possible technique to deal with the problem of pressure has been used in [19] to solve 3-D Navier-Stokes and energy equations in a parallelepiped domain. This method is analogous to the projection method [2] with an elegant iterative process. By applying the above variable changes, equation (2.1) transforms into (2.20) with  $\tilde{T}$  as unknown and the system (3.1a,b,c)-(3.2) becomes

$$\frac{\partial \tilde{v}_z}{\partial t} = \tilde{E} = r \left( \text{Pr} \Delta v_z - \mathbf{V} \cdot \nabla v_z \right) - \frac{\partial \tilde{p}}{\partial z} + \cos(a\phi + b) \text{Pr Ra} \tilde{T} + r F_{v_z}, \quad (3.3a)$$

$$\begin{aligned} \frac{\partial \tilde{v}_r}{\partial t} = \tilde{G} = r \left( \text{Pr} \Delta v_r - \mathbf{V} \cdot \nabla v_r \right) + \frac{\tilde{p}}{r} - \frac{\partial \tilde{p}}{\partial r}, \\ + \sin(c\phi + d) \sin(e\theta + f) \text{Pr Ra} \tilde{T} + r F_{v_r}, \end{aligned} \quad (3.3b)$$

$$\frac{\partial \tilde{v}_\theta}{\partial t} = \tilde{H} = r \left( \text{Pr} \Delta v_\theta - \mathbf{V} \cdot \nabla v_\theta \right) - \frac{1}{r} \frac{\partial \tilde{p}}{\partial \theta} + \sin(c\phi + d) \cos(e\theta) \text{Pr Ra} \tilde{T} + r F_{v_\theta}, \quad (3.3c)$$

$$\frac{1}{r} \frac{\partial \tilde{p}}{\partial t} + \varepsilon \nabla \cdot \tilde{\mathbf{V}} = 0, \quad (3.3d)$$

with the diffusive term  $r \Delta v_z$  and the convective term  $r \mathbf{V} \cdot \nabla v_z$  obtained by replacing  $\tilde{T}$  by  $\tilde{v}_z$  in (2.20b) and (2.20c), and

$$r \Delta v_r = \frac{\partial^2 \tilde{v}_r}{\partial r^2} - \frac{1}{r} \frac{\partial \tilde{v}_r}{\partial r} + \frac{1}{r^2} \frac{\partial^2 \tilde{v}_r}{\partial \theta^2} + \frac{\partial^2 \tilde{v}_r}{\partial z^2} - \frac{2}{r^2} \frac{\partial \tilde{v}_\theta}{\partial \theta}, \quad (3.3e)$$

$$r \Delta v_\theta = \frac{\partial^2 \tilde{v}_\theta}{\partial r^2} - \frac{1}{r} \frac{\partial \tilde{v}_\theta}{\partial r} + \frac{1}{r^2} \frac{\partial^2 \tilde{v}_\theta}{\partial \theta^2} + \frac{\partial^2 \tilde{v}_\theta}{\partial z^2} + \frac{2}{r^2} \frac{\partial \tilde{v}_r}{\partial \theta}, \quad (3.3f)$$

$$r \mathbf{V} \cdot \nabla v_r = \frac{\tilde{v}_r}{r} \frac{\partial \tilde{v}_r}{\partial r} - \frac{\tilde{v}_r^2}{r^2} + \frac{\tilde{v}_\theta}{r^2} \frac{\partial \tilde{v}_r}{\partial \theta} - \frac{\tilde{v}_\theta^2}{r^2} + \frac{\tilde{v}_z}{r} \frac{\partial \tilde{v}_r}{\partial z}, \quad (3.3g)$$

$$r \mathbf{V} \cdot \nabla v_\theta = \frac{\tilde{v}_r}{r} \frac{\partial \tilde{v}_\theta}{\partial r} + \frac{\tilde{v}_\theta}{r^2} \frac{\partial \tilde{v}_\theta}{\partial \theta} + \frac{\tilde{v}_z}{r} \frac{\partial \tilde{v}_\theta}{\partial z}, \quad (3.3h)$$

$$\nabla \cdot \tilde{\mathbf{V}} = \frac{1}{r} \frac{\partial \tilde{v}_r}{\partial r} + \frac{1}{r^2} \frac{\partial \tilde{v}_\theta}{\partial \theta} + \frac{1}{r} \frac{\partial \tilde{v}_z}{\partial z}. \quad (3.3i)$$

The new system to be solved is equation (2.20) coupled with equations (3.3a,b,c,d), with  $\tilde{T}$ ,  $\tilde{v}_r$ ,  $\tilde{v}_\theta$ ,  $\tilde{v}_z$  and  $\tilde{p}$  as unknowns. The system will be solved by the following steps :

(i) First, we calculate  $\tilde{p}^{n+1}$  by using the following explicit scheme on (3.3d) :

$$\tilde{p}^{n+1} = \tilde{p}^n - \delta t \varepsilon r (\nabla \cdot \tilde{\mathbf{V}})^n. \quad (3.4)$$



(ii) With  $\tilde{T}^n$ ,  $\tilde{v}_r^n$ ,  $\tilde{v}_\theta^n$ , and  $\tilde{v}_z^n$ , we deduce  $\tilde{F}^n$  from (2.20) and then find  $\tilde{T}^{n+1}$ , by replacing  $F^n$  by  $\tilde{F}^n$ ,  $T$  by  $\tilde{T}$ , and by taking  $\Lambda_r = \frac{\partial^2}{\partial r^2} - \frac{1}{r} \frac{\partial}{\partial r} + \frac{1}{r^2}$  in (2.4).

(iii) Using  $\tilde{T}^{n+1}$ ,  $\tilde{p}^{n+1}$ ,  $\tilde{v}_r^n$ ,  $\tilde{v}_\theta^n$ , and  $\tilde{v}_z^n$ , we then calculate  $\tilde{E}^{n,n+1}$ ,  $\tilde{G}^{n,n+1}$  and  $\tilde{H}^{n,n+1}$  relative to (3.3a), (3.3b) and (3.3c) respectively.

(iv) We then deduce  $\tilde{v}_z^{n+1}$  by replacing  $F^n$  by  $\tilde{E}^{n,n+1}$ ,  $T$  by  $\tilde{v}_z$ , and use the same operator  $\Lambda_r$  as for  $\tilde{T}^{n+1}$  in (2.4).

(v) For the calculation of  $\tilde{v}_r^{n+1}$  we replace  $F^n$  by  $\tilde{G}^{n,n+1}$ ,  $T$  by  $\tilde{v}_r$  and set  $\Lambda_r = \frac{\partial^2}{\partial r^2} - \frac{1}{r} \frac{\partial}{\partial r}$  in (2.4).

(vi) Finally,  $\tilde{v}_\theta^{n+1}$  is computed by replacing  $F^n$  by  $\tilde{H}^{n,n+1}$ ,  $T$  by  $\tilde{v}_\theta$  and by taking the same operator  $\Lambda_r$  as for  $\tilde{v}_r^{n+1}$  in (2.4).

The right-hand-side  $\tilde{F}^n$  corresponds to  $\tilde{F}$  at the time  $t = n \delta t$ . The computation of  $\tilde{E}^{n,n+1}$ ,  $\tilde{G}^{n,n+1}$  and  $\tilde{H}^{n,n+1}$  is made by using the velocities at the time  $t = n \delta t$ , and the pressure and the temperature at the time  $t = (n+1)\delta t$ . For the stages (iv), (v) and (vi), the operators  $\Lambda_\theta$ ,  $\Lambda_z$  and  $\Lambda_r$  are multiplied by  $\text{Pr}$ .

### 3.2 Evaluation of the method with an analytical solution

In order to assess the method described in Section 3.1 on problem (2.1)-(3.1), we have chosen the exact solutions (2.24) and (2.26a,b,c) for  $T$ ,  $v_r$ ,  $v_\theta$  and  $v_z$ , respectively, and

$$p_{\text{ex}} = \cos(2\theta) r^3 (1 - z^2). \quad (3.5)$$

From these exact solutions, we readily deduce the Dirichlet boundary conditions of the variables and the forcing terms  $F_T$  (see 2.27),  $F_{v_z}$ ,  $F_{v_\theta}$  and  $F_{v_r}$ . The chosen initial conditions are (2.28), for  $T$ , (3.5) for  $p$ , (2.26a,c) perturbed with

$$P_V = 20 (R - r) (z^2 - 1) \cos 5\theta , \quad (3.6)$$

for  $v_r$  and  $v_z$ , and (2.26b) perturbed with  $r P_V$  for  $v_\theta$ . The calculations have been done with  $Pr = Ra = C = R = 1$ ,  $a = b = c = e = 0$ ,  $f = d = \pi / 2$ .

Table 3 shows the convergence and accuracy results of the method, after 2000 time cycles, when  $\delta t = 10^{-2}$  and  $N_r \times K_\theta \times M_z = 10 \times 20 \times 11$ . After this number of iterations the maximum of accuracy has been almost reached. In these calculations we noticed that the maximum error was always located at the collocation points close to the axis. This is certainly a consequence of the variable change used to remove the singularity. We remark that the rate of convergence is connected to the arbitrary constant  $\epsilon$  (occurring in (3.3d)). For this specific problem, with this number of polynomials, and this value of  $\delta t$ , the value  $\epsilon = 30$  was found optimal. An interesting possibility for improving the convergence, would be to employ a technique analogous to [4, p.149] to adjust the coefficient  $\epsilon$  at each time step. Note that the initial conditions are totally different from the final steady solutions. In real physical problems we generally choose the initial conditions to be as close as possible to the expected ones.

### 3.3 Evaluation of the method on two simple physical problems

In this section we shall apply the above method to two simple convective flow problems of incompressible fluids using the real Navier-Stokes and heat equations within the Boussinesq

approximation. The goal is not to study these physical problems but to assess the method by comparing it with two other ones. Thus, we shall have to solve the equation (2.1) with  $F_T = 0$  (corresponding to the heat equation) coupled with equations (3.1) when  $F_{v_r} = F_{v_\theta} = F_{v_z} = b = d = f = 0$  and  $a = c = e = 1$  (corresponding to the Navier-Stokes equation), in the domain  $\Omega_1$ . These equations are written in dimensionless variables with the Prandtl number  $Pr$  and the Rayleigh number  $Ra$  as physical dimensionless parameters. For the comparison with other methods, we have chosen two physical problems which have 2-D solutions. The first generates an axisymmetric solution and the second one a solution independent of the axial direction. The other methods chosen for the comparison, were designed for solving 2-D Navier-Stokes and heat equations. The Rayleigh number  $Ra$  has deliberately been chosen to be small, in order to avoid problems related to the accuracy of each method. In forthcoming sections we shall denote the maximum values of  $v_r$ ,  $v_\theta$ ,  $v_z$ ,  $v_x$  and  $v_y$  by  $v_{r \max}$ ,  $v_{\theta \max}$ ,  $v_{z \max}$ ,  $v_{x \max}$  and  $v_{y \max}$ , respectively. The variables  $v_x$  and  $v_y$  are the velocities in Cartesian coordinates such that  $v_x = v_r \cos \theta - v_\theta \sin \theta$  and  $v_y = v_r \sin \theta + v_\theta \cos \theta$ . As these maxima are calculated at the collocation points particular to each method, small differences are expected in the results.

### 3.3.1 Axisymmetric solution

For this problem, the fluid is differentially heated in a vertical cylinder having rigid walls as boundaries. The axisymmetric convective flow is generated by an axisymmetric non-linear temperature distribution at the initial state. The equations described earlier were solved with  $\phi = 0$  (i.e. gravity parallel to the axis  $r = 0$ ),  $Pr = 1$ , and the boundary and initial conditions

$$v_r = v_\theta = v_z = 0 \quad \text{on } \Gamma_1, \quad (3.7a)$$

$$T = 0 \text{ at } z = 1, \quad T = 1 \text{ at } z = -1, \quad T = (z - 1)^2 / 4 \text{ at } r = R, \quad (3.7b)$$

$$v_r = v_\theta = v_z = 0 \quad \text{at } t = 0, \quad (3.8a)$$

$$T = (z - 1)^2 / 4 \quad \text{at } t = 0. \quad (3.8b)$$

Table 4 gives the values of  $v_{r \max}$  and  $v_{z \max}$ , at different Rayleigh numbers, obtained with the finite volume program PHOENICS [20] in cylindrical coordinates, the finite element code FIDAP [9,10] in Cartesian coordinates and our present method. The calculations were done by taking  $N_r \times M_z = 18 \times 36$  with PHOENICS,  $N_r \times M_z = 17 \times 31$  with FIDAP and  $N_r \times M_z = 13 \times 19$  with our method. Note that for PHOENICS and FIDAP the mesh was regularly spaced. We can observe a perfect agreement between our results and those given by FIDAP and a small discrepancy with PHOENICS which yields about 5% higher values. The error associated with the first-order finite volume approximation used in [20] has the effect of slightly increasing the values of  $v_{r \max}$  and  $v_{z \max}$ . Note that these results were obtained with an optimum mesh size when using FIDAP and PHOENICS. Fig.2 exhibits the velocity and temperature fields when  $Ra = 150$ . We can see that  $v_{z \max}$  is located on the axis.

### 3.3.2 Solution independent of the axial direction

In this section, the fluid is heated from the side in a horizontal cylinder with rigid walls. The convective flow is buoyancy generated by taking  $\phi = \pi / 2$  (i.e. gravity perpendicular to the axis  $r = 0$ ),  $Pr = 1$ , and the boundary and initial conditions

$$v_r = v_\theta = v_z = 0 \quad \text{at the sidewalls } (r=R), \quad (3.9a)$$

$$\frac{\partial v_r}{\partial z} = \frac{\partial v_\theta}{\partial z} = \frac{\partial v_z}{\partial z} = 0 \quad \text{at the endwalls } (z = \pm 1), \quad (3.9b)$$

$$T = \cos \theta \quad \text{on } \Gamma_1, \quad (3.9c)$$

$$v_r = v_\theta = v_z = 0 \quad \text{at } t = 0, \quad (3.10a)$$

$$T = r \cos \theta \quad \text{at } t = 0. \quad (3.10b)$$

By enforcing  $v_z = 0$  in the equations, the solution becomes independent of the axial direction. Table 5 shows the values of  $v_x \max$  and  $v_y \max$ , obtained with  $Ra = 60$  and  $120$ , first by using FIDAP and then our method. The calculations with FIDAP were done by taking a regularly spaced Cartesian grid  $29 \times 29$  and  $N_r \times K_\theta = 13 \times 18$  with our method. As in the previous section, we obtain a good agreement between these two methods. Fig.3 presents the velocity and temperature fields when  $Ra = 120$ .

#### 4. Application to a natural convection problem

In this section the method is illustrated with a convection problem of a differentially heated fluid in a horizontal cylinder having a length  $2H$  and a diameter  $D$  ( $A=D/2H$  is the aspect ratio). The vertical endwalls of the cylinder are maintained at constant temperatures  $T_1$  and  $T_2$  while the horizontal boundary is conducting. The convective flow is generated by the buoyancy force as soon as  $T_2 \neq T_1$ . The intensity of the resulting flow is connected to the magnitude of the difference  $T_2 - T_1$ . All boundaries of the cylinder are rigid with no-slip conditions for the velocities. The mathematical model is given by the same Navier-Stokes and energy equations as used in section 3.3 where  $\varphi = \pi / 2$  (i.e. gravity perpendicular to the axis  $r = 0$ ). These equations are cast in dimensionless form with  $H$ ,  $H^2/\kappa$ ,  $\kappa/H$ , and  $T_2 - T_1$  as characteristic scales for length, time, velocity and temperature, respectively. The resulting dimensionless computational domain is  $\Omega_1$  with  $R = A$ . The physical dimensionless parameters are the Prandtl number  $Pr = \nu / \kappa$  and the Rayleigh number  $Ra = g\alpha H^3(T_2 - T_1) / \kappa \nu$  where  $g$  is the gravitational acceleration,  $\alpha$  the

thermal expansion coefficient,  $\nu$  the kinematic viscosity,  $\kappa$  the thermal diffusivity. The dimensionless boundary and initial conditions are

$$v_r = v_\theta = v_z = 0 \quad \text{at the endwalls } (z = \pm 1) \text{ and the sidewalls } (r = R), \quad (4.1a)$$

$$T = 0 \text{ at } z = 1, \quad T = 1 \text{ at } z = -1, \quad T = 0.5(1 + z) \text{ at } r = R, \quad (4.1b)$$

$$v_r = v_\theta = v_z = 0 \quad \text{at } t = 0, \quad (4.2a)$$

$$T = 0.5(1 + z) \quad \text{at } t = 0. \quad (4.2b)$$

Table 6 shows the values of  $v_{x \max}$ ,  $v_{y \max}$  and  $v_{z \max}$ , obtained with  $Pr = 1$ ,  $A = 1$  and  $Ra = 60, 100$  and  $600$ , first by using the finite element code FIDAP and then our method. For FIDAP we have employed an irregularly spaced Cartesian grid with  $N_x \times N_y \times N_z = 17 \times 17 \times 11$ , similar to the example depicted by a figure in vol.3, section 35-27, of the FIDAP manual [9]. We denote  $N_x$ ,  $N_y$  and  $N_z$  the number of nodes in the  $x$ ,  $y$  and  $z$  directions respectively. For our method all calculations (tables 6 and 7) have been performed with a spatial resolution defined by  $N_r \times K_\theta \times M_z = 13 \times 18 \times 19$  and a time-step  $\delta t$  varying between  $3 \cdot 10^{-3}$  and  $1 \cdot 10^{-3}$  according to the stiffness of the solution. The product  $\delta t \varepsilon$  occurring in (3.4) is maintained at the value 0.2 for all computations related to this section. Table 6 shows good agreement between these two methods. Table 7 summarizes the details of our computations corresponding to  $Pr = 1$ ,  $A = 1$  and  $Ra$  between 1000 and 13000. The starting condition (4.2) has been used only for the lowest Rayleigh number. For the others, the starting condition is the solution calculated with a lower  $Ra$ . With the chosen number of polynomials, on a Cray XMP computer, the computational cost for one time-step is 0.081 second. Since the goal was to illustrate the method and its applications rather than undertake an exhaustive study, we did not try to explore the solutions for  $Ra \geq 13000$ . The physical study of this problem has been carried out in [21-23] with other parameters by means of a finite difference method. Table 7 shows in particular that the time step

decreases with increasing  $Ra$  which leads to a corresponding increase of the number of cycles. However, even with 6000 cycles the total CPU time remains reasonable (486 sec.). Note that for high  $Ra$  we have stopped our calculations when the divergence (corresponding to (3.1d))  $\nabla \cdot V \approx 10^{-5}$ . For these values of  $\nabla \cdot V$ , we noticed that the values of the velocity and temperature fields do not change significantly when decreasing the divergence to lower values. This fact was independently pointed out in [24]. Figures 4 and 5 exhibit the velocity and temperature fields when  $Ra = 13000$ . The projection of these fields in the  $(r, z)$ -planes is shown in figure 4 for  $\theta$  equal to  $0^\circ$ ,  $40^\circ$  and  $80^\circ$ . At  $\theta = 0^\circ$ , the flow has one roll in each corner. At  $40^\circ$  and  $80^\circ$ , it consists of roughly one cell with a contraction in the middle. Fig. 5 exhibits the fields at various cross-sections  $(r, \theta)$ . At  $z = 0.76$ , i.e. close to the hot endwall, the flow is ascending and perfectly symmetrical to the descending flow at  $z = -0.76$ , i.e. close to the cold endwall. At  $z = 0$ , it is mainly directed from the side to the middle with two secondary flows in the vicinity of the wall crossing the median axis parallel to the gravity. Note that for  $Ra = 13000$ , the flow encountered could be defined as a "Boundary Layer Driven Regime", as proposed by [23].

## 5. Conclusion

A Fourier-Chebyshev pseudospectral method has been proposed for solving steady 3D Navier-Stokes and heat equations in cylindrical cavities. The principal computational difficulties in such geometries come from the presence of the singularity at the axis and the number of collocation points required to accurately represent the solution. Concerning the first difficulty, two techniques have been considered and evaluated. One is based on a variable change and the other on a special distribution of the collocation points. The technique using the variable change has been found more adapted to the general method. Moreover, the use of a pseudospectral method admits an accurate representation of the solution with a small number of collocation points.

This paper has been focused on the solution of steady problems. Therefore, difficulties connected to the incompressibility condition and the pressure could be efficiently circumvented by means of the artificial compressibility method. The latter, coupled with the use of the ADI procedure in the general method leads to a very fast and accurate algorithm for computing steady 3-D incompressible flows. However, for an extension of this method to unsteady problems, the present way to deal with pressure could be time consuming, due to the resulting iterative process. A better technique to extend it to time dependent problems, might be the use of a semi-direct method as in [19], to satisfy the divergence free field. Finally, the application of our method to a natural convection problem, has shown that this technique can cope efficiently with relatively large Rayleigh numbers.

**Acknowledgments :** This research was supported by NASA's Microgravity Science and Application Division under grants DO14 and NAG8-790, and by the state of Alabama through the Center for Microgravity and Materials Research at the University of Alabama in Huntsville and the Alabama Supercomputer Network. The authors especially thank Dr. R. Peyret and Dr. P. Bontoux for their help in the development of the method. They would like to acknowledge Prof. F. Rosenberger and Dr. J.I.D. Alexander who proposed and encouraged this work and Dr. A. Nadarajah and Dr. St. Krukowski for useful discussions during this research. We also thank the reviewers for their helpful comments which were incorporated into the article.



## References

1. D. Gottlieb and S.A. Orszag, *Numerical Analysis of Spectral Methods : Theory and Application*, SIAM Monograph no. 26, SIAM, Philadelphia, U.S.A. (1977).
2. R. Peyret and T.D. Taylor, *Computational Methods for Fluid Flow*, Springer Verlag, New-York (1983).
3. R. Peyret, Introduction to spectral methods, *Computational Fluid Dynamics, Lecture series* 1986-04, *Von Karman Institute for Fluid Dynamics*, Rhode-St-Genese, Belgium, March 3-7, (1986).
4. C. Canuto, M.Y. Hussaini, A. Quarteroni and T.A. Zang, *Spectral Methods in Fluids Dynamics*, Springer-Verlag, (1988).
5. J. Ouazzani and R. Peyret, A pseudo-spectral solution of binary gas mixture flows, *Notes on Numerical Fluid Mechanics*, (Edited by M. Pandolfi and R. Piva), **7**, 275-282, Vieweg Verlag, Braunschweig (1984).
6. L. Kleiser and U. Shumann, Treatment of incompressibility and boundary conditions in 3-D numerical simulations of plane channel flows, *Proc. 3rd GAMM Conf. Numer. Methods in Fluid Mech.*, ( Edited by E.H. Hirschel ), 165-173, Vieweg, Braunschweig (1980).
7. L. S. Tuckerman, Divergence-free velocity fields in nonperiodic geometries, *J. comput. phys*, **80**, 403-441 (1989).

8. P. Le Quéré and J. Pécheux, A three-dimensional pseudo-spectral algorithm for the computation of convection in a rotating annulus, ICOSAHOM'89, Como, Italy, June 26-29, (1989).
9. M.S. Engelman, FIDAP Fluid Dynamics Analysis Program User / Theoretical Manual, Control Data Corporation, version 5, (1989).
10. M.S. Engelman and R.L. Sani, Proceedings of the ASME Convection in Enclosures Conference, (1983).
11. S.A. Orszag and A.T. Patera, Secondary instability of wall-bounded shear flows, *J. Fluid Mech.*, **128**, 347-385 (1983).
12. D. Schnack and J. Killeen, Nonlinear two-dimensional magnetohydrodynamic calculations, *J. Comput. Phys.*, **35**, 110-145 (1980).
13. S.S. Leong and G. De Vahl Davis, Natural convection in a horizontal cylinder, Numerical Methods in Thermal Problems I (Edited by R.W. Lewis and K. Morgan), 287-296, Pineridge (1979).
14. C. Temperton, Fast mixed-radix real Fourier transforms, *J. Comp. Phys.*, **52**, 340-350 (1983).
15. P. Concus and G.H. Golub, Use of fast direct methods for the efficient numerical solution of nonseparable elliptic equations, *SIAM J. Numer. Anal.*, **10**, No. 6, (1973).

16. A. Randriamampianina, Simulation des mouvements convectifs et transferts thermiques en milieu confiné, Memoire de these, Univ. d'Aix-Marseille II, Marseille (1984).
17. C. Basdevant, M. Deville, P. Haldenwang, J.M. Lacroix, J. Ouazzani, R. Peyret, P. Orlandi and A.T. Patera, Spectral and finite difference solutions of Burgers equation, *Computers and fluids*, **14**, 23-41 (1986).
18. R.B. Bird, W.E. Stewart and E.N. Lightfoot, *Transport Phenomena*, John Wiley and Sons, Inc., New York London (1960).
19. P. Haldenwang, G. Labrosse, S. Abboudi and M. Deville, Chebyshev 3D spectral and 2D Pseudospectral Solvers for the Helmholtz Equation, *J. Comput. Phys.*, **55**, 115-128 (1984).
20. H.I. Rosten and D.B. Spalding, Cham Report TR/200, The PHOENICS User Manual, (1987).
21. C. Smutek, P. Bontoux, B. Roux, G.H. Schiroky, A.C. Hurford, F. Rosenberger and G. De Vahl Davis, Three-dimensional convection in horizontal cylinders: numerical solutions and comparison with experimental and analytical results, *Num. Heat Transfer*, **8**, 613-631 (1985).
22. P. Bontoux, C. Smutek, B. Roux and J.M. Lacroix, Three-dimensional buoyancy-driven flows in cylindrical cavities with differentially heated endwalls, *J. Fluid Mech.*, **169**, 211-227 (1986).

23. P. Bontoux, C. Smutek, A. Randriamampianina, B. Roux, G. P. Extrémet, A. C. Hurford, F. Rosenberger and G. De Vahl Davis, Numerical solutions and experimental results for three dimensional buoyancy driven flows in tilted cylinders, *Adv. Space Res.*, **6**, No. 5, 155-160, Pergamon, (1986).
24. K Gustafson and K. Halasi, Vortex dynamics of cavity flows, *J. Comp. Phys.*, **64**, 279-319 (1986).

## **Table headings**

Table 1 - Convergence and accuracy after 200 time cycles for methods I, II and III.

Table 2 - Convergence and accuracy for method II.

Table 3 - Convergence and accuracy for problem of section 3.2.

Table 4 - Accuracy for problem of section 3.3.1.

Table 5 - Accuracy for problem of section 3.3.2.

Table 6 - Accuracy for problem of section 4.

Table 7 - Results regarding the problem of section 4.

**Table 1**

Method	$N_r \times K_\theta \times M_z$	$\delta t$	$R_T$ (for I & III) $R_{\tilde{T}}$ (for II)	$E_T^{L2}$	$E_T^{Sup}$
I	$10 \times 20 \times 13$	$9.0 \cdot 10^{-3}$	$7.65 \cdot 10^{-10}$	$1.24 \cdot 10^{-11}$	$8.36 \cdot 10^{-11}$
	$21 \times 20 \times 13$	$4.0 \cdot 10^{-3}$	$1.22 \cdot 10^{-4}$	$1.33 \cdot 10^{-6}$	$2.47 \cdot 10^{-5}$
II	$10 \times 20 \times 13$	$1.2 \cdot 10^{-2}$	$4.96 \cdot 10^{-12}$	$8.38 \cdot 10^{-13}$	$7.37 \cdot 10^{-12}$
	$21 \times 20 \times 13$	$4.0 \cdot 10^{-3}$	$1.05 \cdot 10^{-5}$	$7.32 \cdot 10^{-7}$	$2.00 \cdot 10^{-6}$
III	$26 \times 10 \times 13$	$1.6 \cdot 10^{-2}$	$1.82 \cdot 10^{-11}$	$2.92 \cdot 10^{-9}$	$1.72 \cdot 10^{-8}$
	$46 \times 10 \times 13$	$1.0 \cdot 10^{-2}$	$9.60 \cdot 10^{-10}$	$2.51 \cdot 10^{-11}$	$1.80 \cdot 10^{-10}$

**Table 2**

$N_r \times K_\theta \times M_z$	$\sigma$	$\delta t$	Number of cycles	$R_T$	$E_T^{L2}$	$E_T^{Sp}$
$9 \times 16 \times 9$	0.5	$2.0 \cdot 10^{-2}$	50	$8.21 \cdot 10^{-7}$	$3.98 \cdot 10^{-3}$	$1.76 \cdot 10^{-2}$
$10 \times 20 \times 11$	0.5	$1.2 \cdot 10^{-2}$	200	$4.68 \cdot 10^{-12}$	$4.12 \cdot 10^{-13}$	$1.23 \cdot 10^{-12}$
$10 \times 20 \times 11$	0.75	$1.2 \cdot 10^{-2}$	300	$1.60 \cdot 10^{-11}$	$1.16 \cdot 10^{-11}$	$1.07 \cdot 10^{-10}$
$10 \times 20 \times 11$	1.0	$1.2 \cdot 10^{-2}$	400	$7.24 \cdot 10^{-9}$	$9.37 \cdot 10^{-9}$	$1.01 \cdot 10^{-7}$
$13 \times 24 \times 13$	0.5	$0.8 \cdot 10^{-2}$	300	$1.78 \cdot 10^{-12}$	$1.68 \cdot 10^{-12}$	$5.64 \cdot 10^{-12}$

**Table 3**

$\vartheta$	$\varepsilon$	$R_{\vartheta}^{\sim}$	$E_{\vartheta}^{L2}$	$E_{\vartheta}^{Sup}$
T	30	$9.13 \cdot 10^{-13}$	$7.63 \cdot 10^{-13}$	$2.23 \cdot 10^{-12}$
	25	$9.92 \cdot 10^{-13}$	$7.74 \cdot 10^{-13}$	$2.29 \cdot 10^{-12}$
	20	$1.12 \cdot 10^{-12}$	$8.33 \cdot 10^{-13}$	$2.43 \cdot 10^{-12}$
$v_z$	30	$2.19 \cdot 10^{-9}$	$1.47 \cdot 10^{-8}$	$1.53 \cdot 10^{-7}$
	25	$7.52 \cdot 10^{-9}$	$5.85 \cdot 10^{-8}$	$6.30 \cdot 10^{-7}$
	20	$2.38 \cdot 10^{-8}$	$2.24 \cdot 10^{-7}$	$2.48 \cdot 10^{-6}$
$v_r$	30	$5.47 \cdot 10^{-11}$	$2.46 \cdot 10^{-10}$	$1.57 \cdot 10^{-9}$
	25	$1.87 \cdot 10^{-10}$	$9.51 \cdot 10^{-10}$	$6.29 \cdot 10^{-9}$
	20	$5.91 \cdot 10^{-10}$	$3.52 \cdot 10^{-9}$	$2.42 \cdot 10^{-8}$
$v_{\theta}$	30	$9.08 \cdot 10^{-11}$	$8.70 \cdot 10^{-10}$	$6.42 \cdot 10^{-9}$
	25	$3.06 \cdot 10^{-10}$	$3.37 \cdot 10^{-9}$	$2.59 \cdot 10^{-8}$
	20	$9.56 \cdot 10^{-10}$	$1.25 \cdot 10^{-8}$	$1.00 \cdot 10^{-7}$
p	30	$6.04 \cdot 10^{-6}$	$1.32 \cdot 10^{-7}$	$9.86 \cdot 10^{-7}$
	25	$2.07 \cdot 10^{-5}$	$5.19 \cdot 10^{-7}$	$4.00 \cdot 10^{-6}$
	20	$6.59 \cdot 10^{-5}$	$1.94 \cdot 10^{-6}$	$1.56 \cdot 10^{-5}$



**Table 4**

	PHOENICS		FIDAP		SPECTRAL	
Ra	V <sub>z</sub> max	V <sub>r</sub> max	V <sub>z</sub> max	V <sub>r</sub> max	V <sub>z</sub> max	V <sub>r</sub> max
10	1.77 10 <sup>-2</sup>	4.15 10 <sup>-3</sup>	1.66 10 <sup>-2</sup>	3.98 10 <sup>-3</sup>	1.66 10 <sup>-2</sup>	3.96 10 <sup>-3</sup>
100	1.91 10 <sup>-1</sup>	4.50 10 <sup>-2</sup>	1.80 10 <sup>-1</sup>	4.28 10 <sup>-2</sup>	1.80 10 <sup>-1</sup>	4.23 10 <sup>-2</sup>
150	3.02 10 <sup>-1</sup>	6.90 10 <sup>-2</sup>	2.82 10 <sup>-1</sup>	6.64 10 <sup>-2</sup>	2.82 10 <sup>-1</sup>	6.59 10 <sup>-2</sup>

**Table 5**

	FIDAP		SPECTRAL	
Ra	v <sub>x</sub> max	v <sub>y</sub> max	v <sub>x</sub> max	v <sub>y</sub> max
60	1.39	1.41	1.38	1.40
120	2.66	2.69	2.62	2.68

**Table 6**

Ra	FIDAP			SPECTRAL		
	V <sub>x</sub> max	V <sub>y</sub> max	V <sub>z</sub> max	V <sub>x</sub> max	V <sub>y</sub> max	V <sub>z</sub> max
60	0.10	0.74	0.87	0.10	0.71	0.86
100	0.18	1.17	1.44	0.17	1.17	1.43
600	1.44	5.20	6.50	1.38	5.52	6.96

**Table 7**

Ra	$\delta t$	Number of cycles	$\nabla \cdot V$ (3.1d)	$v_{r \max}$	$v_{\theta \max}$	$v_{z \max}$	Initial condition
1000	$3.0 \cdot 10^{-3}$	2000	$1.1 \cdot 10^{-4}$	7.82	7.91	9.89	Sol. (4.2)
2000	$3.0 \cdot 10^{-3}$	3000	$5.0 \cdot 10^{-5}$	11.72	12.45	14.82	Sol. at Gr=1000
3000	$3.0 \cdot 10^{-3}$	4000	$2.2 \cdot 10^{-5}$	14.29	16.20	18.26	Sol. at Gr=2000
4000	$3.0 \cdot 10^{-3}$	4000	$3.0 \cdot 10^{-5}$	17.05	19.45	20.99	Sol. at Gr=3000
5000	$3.0 \cdot 10^{-3}$	4000	$4.0 \cdot 10^{-5}$	19.40	22.09	23.29	Sol. at Gr=4000
6000	$3.0 \cdot 10^{-3}$	4000	$5.0 \cdot 10^{-5}$	21.53	24.80	25.35	Sol. at Gr=5000
7000	$2.0 \cdot 10^{-3}$	4000	$6.4 \cdot 10^{-5}$	23.44	27.33	27.39	Sol. at Gr=6000
8000	$2.0 \cdot 10^{-3}$	4000	$8.8 \cdot 10^{-5}$	25.18	29.59	29.26	Sol. at Gr=7000
9000	$2.0 \cdot 10^{-3}$	4000	$1.3 \cdot 10^{-4}$	26.77	31.62	31.01	Sol. at Gr=8000
10000	$1.5 \cdot 10^{-3}$	5000	$3.7 \cdot 10^{-5}$	28.24	33.44	32.65	Sol. at Gr=9000
11000	$1.5 \cdot 10^{-3}$	5000	$6.1 \cdot 10^{-5}$	29.62	35.61	34.21	Sol. at Gr=10000
12000	$1.5 \cdot 10^{-3}$	5000	$9.6 \cdot 10^{-5}$	30.90	37.69	35.68	Sol. at Gr=11000
13000	$1.0 \cdot 10^{-3}$	6000	$2.9 \cdot 10^{-5}$	32.15	39.66	37.09	Sol. at Gr=12000

## Figure legends

- Fig. 1 Geometry of the enclosure and frame of reference.
- Fig. 2 Problem of section 3.3.1 : (a) velocity field, (b) temperature field for  $Ra = 150$ .
- Fig. 3 Problem of section 3.3.2 : (a) velocity field, (b) temperature field for  $Ra = 120$ .
- Fig. 4 Problem of section 4 : (a) velocity field, (b) temperature field, in the  $(r,z)$  planes, at  $Ra = 13000$  for  $\theta = 0^\circ, 40^\circ$  and  $80^\circ$ .
- Fig. 5 Problem of section 4 : (a) velocity field, (b) temperature field, in the  $(r,\theta)$  planes, at  $Ra = 13000$  for  $z = 0.76, 0$  and  $-0.76$ .

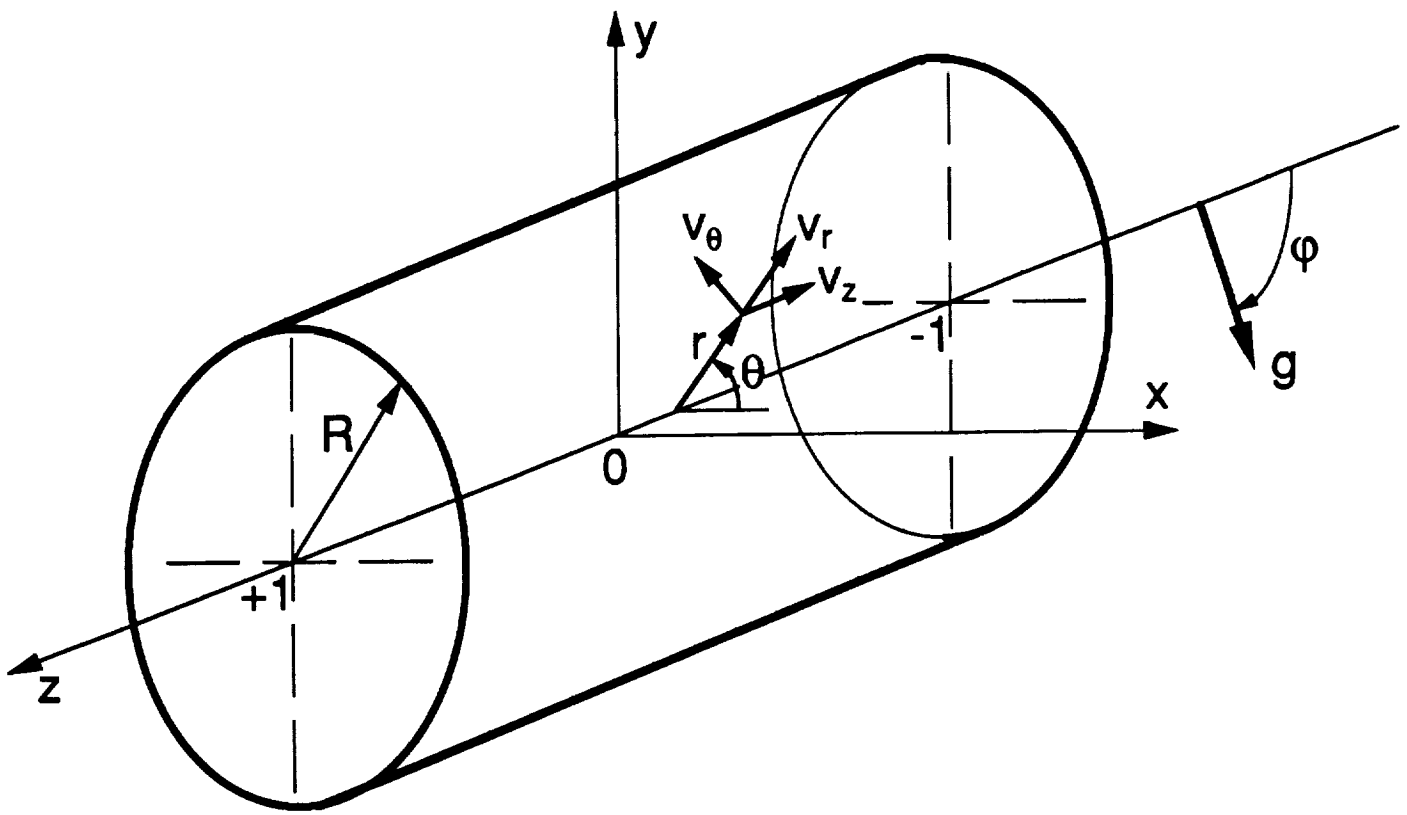
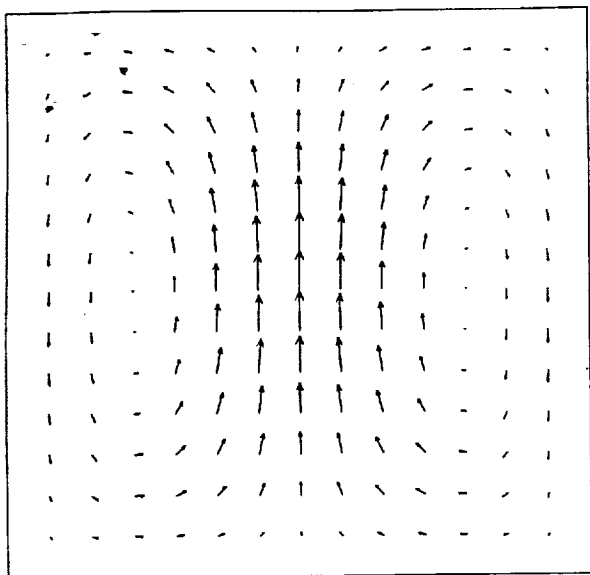
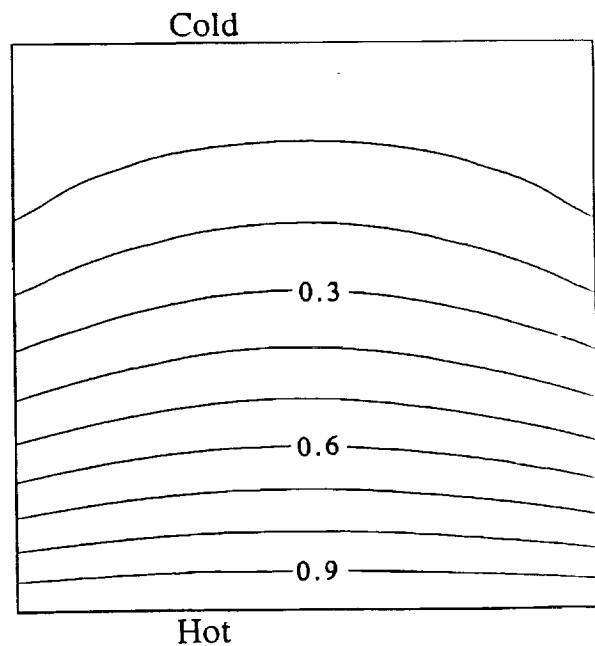
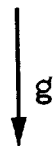


Fig. 1

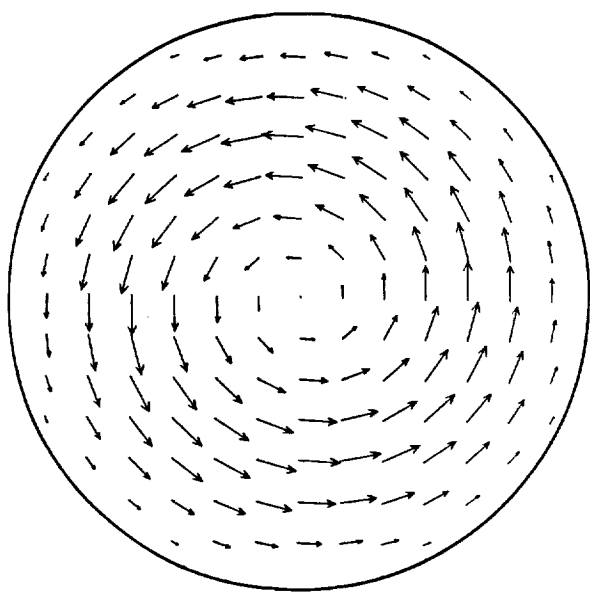


(a)

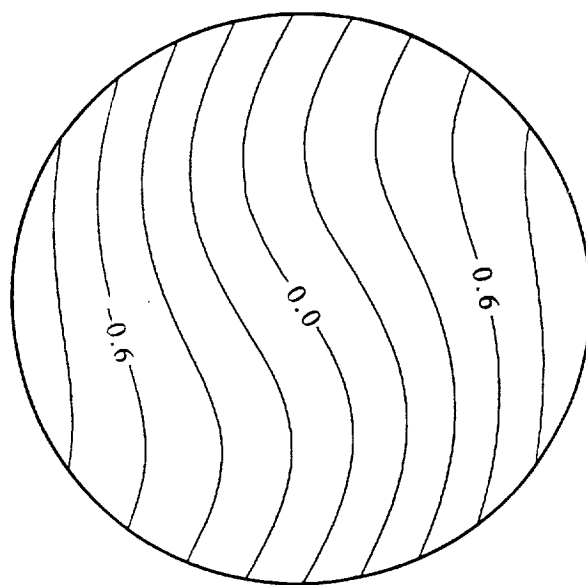


(b)

**Fig. 2**

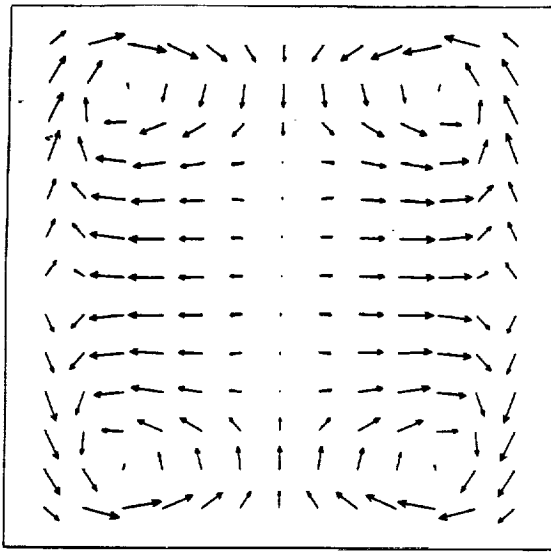


(a)

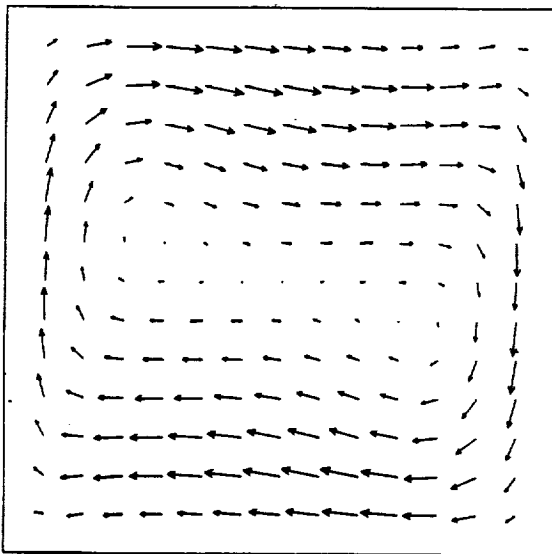
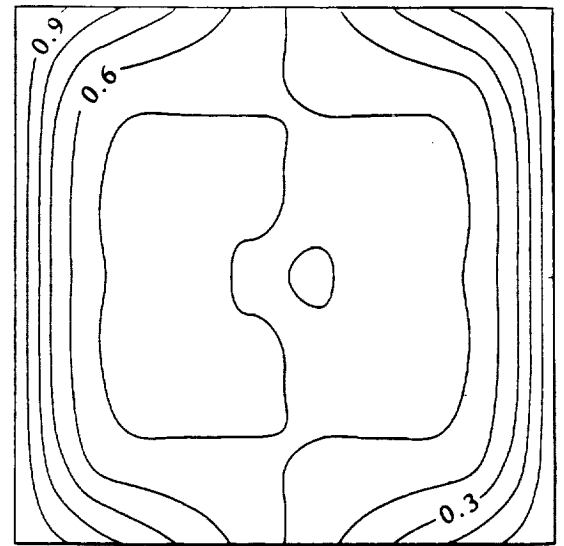


(b)

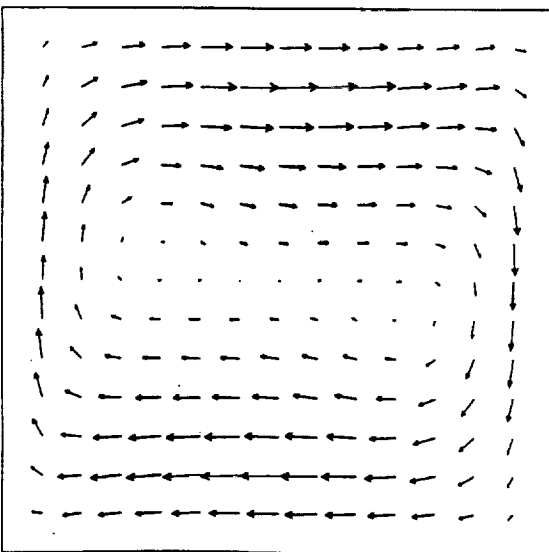
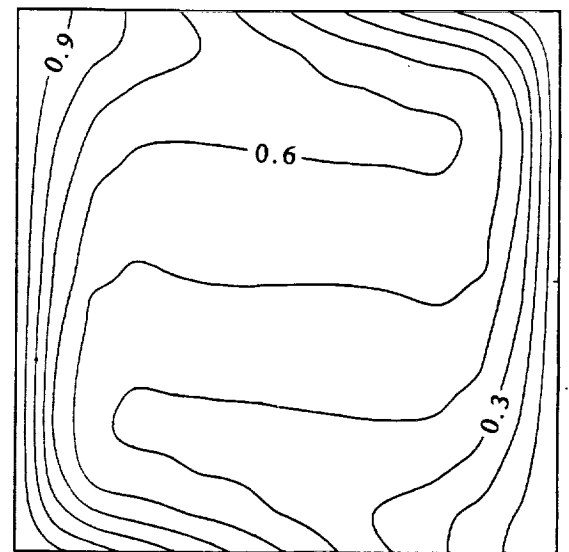
**Fig. 3**



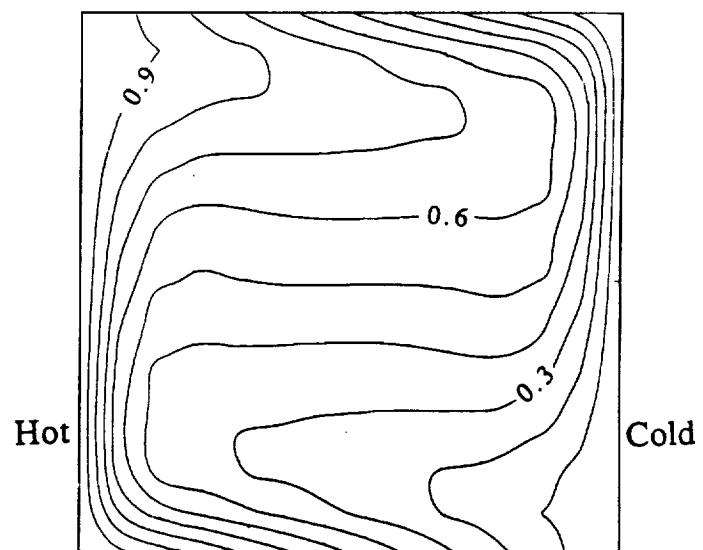
$\theta = 0^\circ$



$\theta = 40^\circ$



$\theta = 80^\circ$



(a)

(b)

Fig. 4



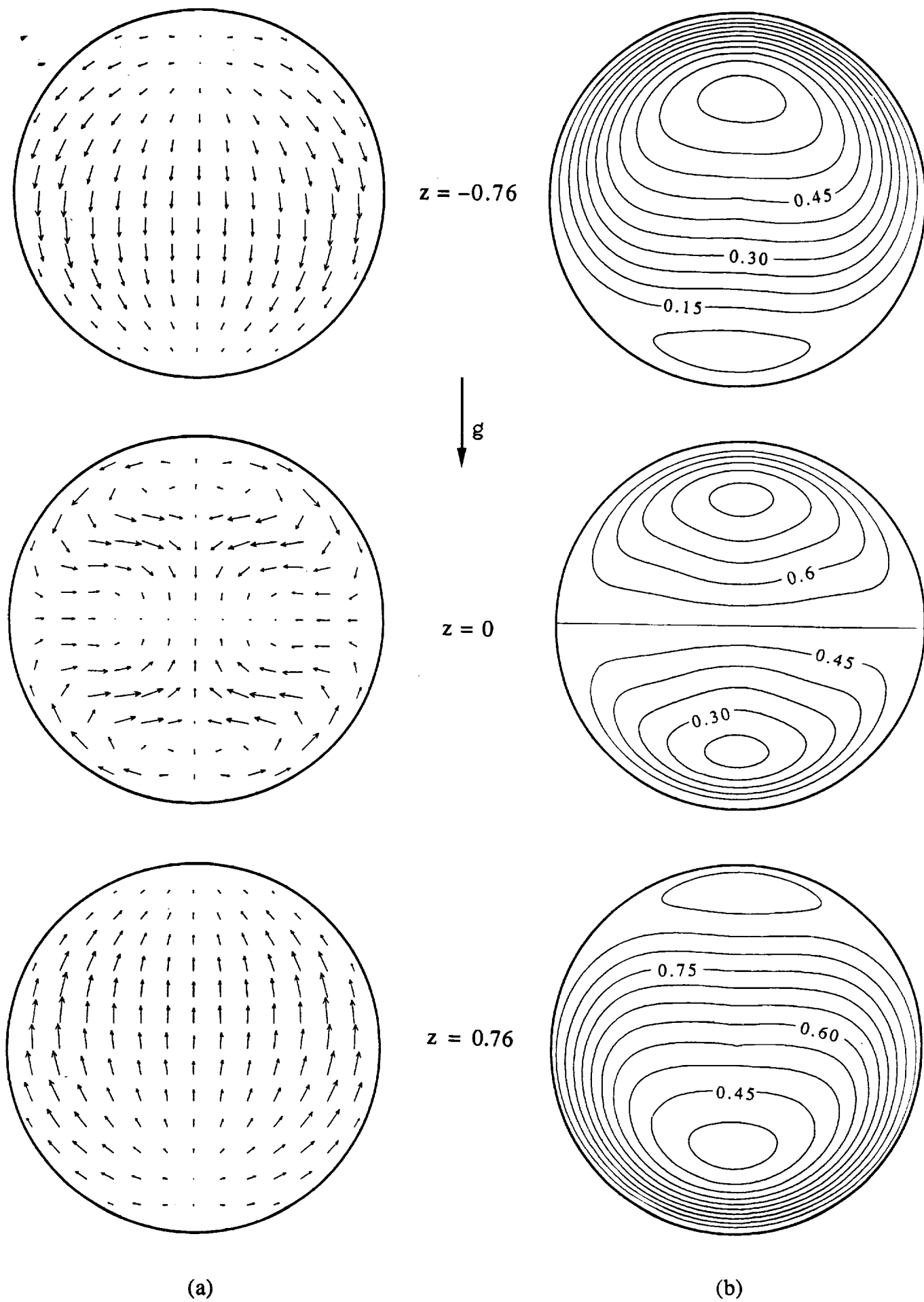


Fig. 5